

Unlocking ultrastrong high-temperature ceramics: Beyond Equimolar Compositions in High Entropy Nitrides

O.V. Pshyk^{a,b,c,d*}, A. Vasylenko^e, P. Küttel^f, B. Wicher^{b,g}, P. Schweizer^a, J. Michler^a, T.E.J. Edwards^a

a Empa — Swiss Federal Laboratories for Materials Science and Technology, Laboratory for Mechanics of Materials and Nanostructures, Thun 3602, Switzerland

b Thin Film Physics Division, Department of Physics (IFM), Linköping University, 581 83 Linköping, Sweden

c NanoBioMedical Centre, Adam Mickiewicz University, Poznań, Poland

d Empa — Swiss Federal Laboratories for Materials Science and Technology, Laboratory for Surface Science and Coating Technology, Dübendorf 8600, Switzerland

e Department of Chemistry, University of Liverpool, Liverpool, United Kingdom

f Alemnis AG, Schorenstrasse 39, 3645 Gwatt, Switzerland

g Faculty of Materials Science and Engineering, Warsaw University of Technology, 02-507 Warsaw, Poland

* Corresponding author: oleksandr.pshyk@empa.ch

Traditionally, increasing compositional complexity and chemical diversity of high entropy alloy ceramics whilst maintaining a stable single-phase solid solution has been a primary design strategy for the development of new ceramics. However, only a handful have shown properties that justify the increased alloying content. Here, we unveil a groundbreaking strategy based on deviation from conventional equimolar composition towards non-equimolar composition space, enabling tuning the metastability level of the supersaturated single-phase solid solution. By employing high-temperature micromechanical testing of refractory metal-based high entropy nitrides, we found that the activation of an additional strengthening mechanism upon metastable phase decomposition propels the yield strength of a non-equimolar nitride at 1000 °C to a staggering 6.9 GPa, that is 30 % higher than the most robust equimolar nitride. We show that the inherent instability triggers the decomposition of the solid solution with non-equimolar

composition at high temperatures, inducing strengthening due to the coherency stress of a spinodally modulated structure, combined with the lattice resistance of the product solid solution phase. In stark contrast, the strength of equimolar systems, boasting diverse chemical compositions, declines as a function of temperature due to the weakening of the lattice resistance and the absence of other strengthening mechanisms.

Introduction

Refractory metal based nitrides belong to the broad family of refractory ceramic materials (a set of carbides, nitrides and borides of the group IV and V transition metals); because of their ultra-high melting temperatures (T_m above ~ 3000 °C) and phase stability they represent the only suitable class of materials available for a diverse range of mechanically loaded applications where components or tools are subjected to the most extreme of operating environments¹. Delving into high entropy ceramics, the number of possibilities for the exploration of refractory nitrides² is much greater. In such multicomponent systems composed of at least five principal binary ceramics, a high configurational entropy (set here by a disordered multi-cation sublattice – assuming that the anion sublattice remains intact) is expected to produce a preference for single-phase solid solutions with simple crystal structures. The presence of many chemically distinct atoms on the metal sublattice produce attractive effects, such as sluggish diffusion and considerable lattice distortion, amongst others³, leading to properties often highly surpassing those of the constituent conventional ceramic components^{3,4}. However, although many studies focus on maximizing configurational entropy (using equimolar ratios of elements), indeed successfully achieving stabilization of single phase solid solution in high-entropy oxides⁵, the impact of configurational entropy on the solid solution phase stability may have been overestimated in metallic alloys^{6,7} and nitrides^{8,9} – configurational entropy may not even be a vital parameter for the design of multicomponent alloys and ceramics with superior properties^{10–12} (Supplementary Note 1). The vast composition space of metastable non-equiatom high-entropy ceramics instead provides even more ways for exploration of new ceramics featuring complex phase transformation sequences upon metastable phase decomposition¹³.

High-temperature mechanical properties are crucial for operation of ceramics in extreme environments¹⁴, yet have been little studied thus far in high entropy ceramics¹⁵. Although the unique mechanical properties of high entropy ceramics are foremost determined by solid solution strengthening among other beneficial mechanisms (see Supplementary Note 2), less attention has been placed on the stability of this mechanism at high temperature, limiting the potential impact of these materials in applications. Inherent metastability of multicomponent nitrides¹⁶, in turn, can allow to trigger different strengthening mechanisms particularly when exposed to mechanical and thermal loads leading to higher strength and damage tolerance. The remarkable improvement of mechanical properties of conventional nitrides due to the formation of three-dimensional nanostructure¹⁷ or precipitation of two-dimensional atomic-plane-thick

Guinier-Preston (GP) zones¹⁸ upon decomposition of single phase solid solutions are proofs of the concept of metastability tuning in high entropy nitrides.

Here, we demonstrate that tuning metastability of high-entropy nitride ceramic thin films by deviating from equimolar metal ratios toward non-equimolar composition space allows to decrease the stability of the solid solution thus enabling its decomposition at elevated temperature. This entails two key benefits: coherency strain strengthening due to a dual-phase isostructural nanostructure (the spinodally decomposed) and retained solid solution hardening of the product high entropy nitride phase. This combination of contributions leads to good retention of high strength at elevated temperatures. At the same time, we see that maximization of configurational entropy in equimolar high entropy nitrides does not maintain high strength at elevated temperature. Due to the relative stability of all equimolar high-entropy nitrides at high temperatures, strength-inducing phase transformations are absent or insufficient to retain high strength in the studied temperature range.

Results

Refractory-metal-based pentanary (TiHfNbVZr)N, hexanary (TiHfNbVZrTa)N, and heptanary (TiHfNbVZrTaW)N thin films, 6 μm thick, were grown by DC magnetron sputtering in an industrial system on (0001) single crystalline sapphire substrates; low and high additions of Al to the pentanary system were enabled by a hybrid HiPIMS/DCMS co-sputtering process. The fraction of metal elements on the cation sublattice was determined by XPS and ToF-ERDA: pentanary (Ti_{0.23}Hf_{0.15}Nb_{0.17}V_{0.21}Zr_{0.24})N, hexanary (Ti_{0.23}Hf_{0.15}Nb_{0.13}V_{0.14}Zr_{0.21}Ta_{0.14})N, heptanary (Ti_{0.17}Hf_{0.11}Nb_{0.14}V_{0.14}Zr_{0.16}Ta_{0.11}W_{0.17})N, hexanary 'Al-low' (Ti_{0.21}Hf_{0.13}Nb_{0.14}V_{0.18}Zr_{0.20}Al_{0.14})N and hexanary 'Al-high' (Ti_{0.13}Hf_{0.07}Nb_{0.07}V_{0.10}Zr_{0.12}Al_{0.51})N, see Supplementary Material 1. Similarly, the anion sublattice is almost fully occupied with N, with a low amount of vacancies; more details about microstructure and elemental composition of the as-deposited films are given in our previous report¹¹.

All nitrides with equimolar metal ratios retain the single phase structure upon annealing up to 1200 °C demonstrating XRD patterns with peaks corresponding to the B1-NaCl-type phase structure, with low intensity shoulders to (111) and (200) peaks (Fig. S1). Annealing at any higher temperature results in the oxidation of the thin film surface (as evident for heptanary thin films after annealing at 1200 °C, Fig.1b), which makes the assessment of high entropy nitride hardness impossible. However, the hexanary Al-high single-phase solid solution undergoes decomposition at 900 °C already, evident as strong left- and right-hand shoulders to

the (111) and (200) peaks, see Fig. 1a; this indicates formation of additional B1-NaCl phases with a small difference in lattice parameters compared to the original (matrix) phase. XRD patterns showing this for two key representative compositions are shown in Fig. 1a-b, while the remainder cases are given in Fig. S1. The above confirms the targeted stability trend realized by tuning composition. *Ab initio* density-functional theory (DFT) calculation of formation energy for the pentanary system and hexanary system with different fractions of Al on the metal sublattice predicts all compositions to be metastable against decomposition to binary or ternary components (Fig. 1c). Importantly, the driving force to decomposition increases as a function of Al fraction, which is in agreement with experiment – without considering the kinetics of the decomposition process that can be significantly altered by Al content or upon the onset of decomposition. Nevertheless, XRD patterns (Fig. 1a, b, Fig. S1) indicate all as-deposited films are single-phase B1-NaCl-structured solid solutions, exhibiting dense fine-fibrous microstructures with column diameters of 80-100 nm and mixed polycrystalline orientations, typical for refractory-metal-based nitrides¹¹. In short, we have synthesized high-entropy nitrides with approximately equimolar, and non-equimolar, metal atom ratios. However, due to the high thermodynamic driving force to decomposition, the non-equimolar solid solution decomposed at elevated temperature while all equimolar solid solutions are relatively more stable (see TEM below). An evaluation of mechanical properties by nanoindentation after annealing, Fig. 1d, reveals good retention of as-deposited hardness up to at least 1100 °C in all conditions, with a minor (<10 %) improvement in hardness seen in the refractory pentanary and hexanary nitrides. However, the Al-high and heptanary systems showed even greater improvement with highest hardness after annealing at 1000 °C (42.6 ± 2.3 GPa) and 1100 °C (44.6 ± 1.9 GPa), respectively. Scanning transmission electron microscopy (STEM) of the highest hardness conditions is carried out to understand the microstructural evolution generating such performance improvements – the as-deposited conditions having been previously characterized¹¹. Whilst the pentanary nitride annealed at 1000 °C displays an unchanged columnar microstructure, Fig. S2a, local chemical segregation across the metal sublattice is evidenced by atomic resolution high-angle annular dark field (HAADF) image, Fig. 2a. The heptanary nitride annealed at 1100 °C exhibits grain-scale segregation, in particular of W (Fig. S2b, Fig. S4), a considerable density of twin boundaries, Fig. 2b, as well as atomic-scale segregation inside the grain, Fig. 2b insert, but no evidence of W-rich Guinier Preston zones previously reported for W-doped ternary nitride (Ti,Al)N¹⁸. Finally, both Al-containing nitrides displayed significant nano-scale chemical segregation after annealing at 1200 °C, Fig. 2c-f and Fig. S5, despite the selected area electron diffraction (SAED) patterns showing only reflections matching the B1-NaCl structure

phase (Fig. S6). EDS mapping (Fig. S5) and EDS line scans (Fig. S7, Fig. 2d, f inserts) reveal separation of all refractory metals from Al between the two contrasting isostructural domains with a modulation wavelength of the order 3.5 ± 0.4 nm for hexanary 'Al-low' and 12.2 ± 2.2 nm hexanary 'Al-high' films. Such decomposition of supersaturated solid solution into coherent cubic nanodomains via spinodal mechanism is typical for Al containing refractory metal nitrides¹⁷. However, to the best of our knowledge, this is the first convincing evidence of such a decomposition in high entropy nitrides, especially in the Al-low system with a relatively low thermodynamic driving force to decomposition.

High-temperature microcompression is carried out to capture mechanical performance and assess the effectiveness of nitride microstructure strategies in conditions approximating extreme applications. Micro-pillars ~ 1.8 μm in diameter, Fig. S8, produced by focused ion beam (FIB) milling, where the height is less than the coating thickness, are compressed *in vacuo* at six temperatures, from room temperature (~ 25 °C) to 1000 °C, using a flat conductive diamond punch. Compressive yield strengths using a 1% strain criterion, σ_y , Fig. 3a, indicate initially greater room temperature strength of the pentanary and hexanary Al-high systems ($\sigma_y \sim 11$ – 12 GPa), whilst all other equimolar systems have $\sigma_y \sim 8$ – 9 GPa. Nevertheless, all such pillars fail by catastrophic brittle fracture; this is seen in stress-strain curves, Fig. 3b, and *post-mortem* SEM images, see Fig. S9, which includes all other test temperatures also. In the 500 to 800 °C range, all systems are softer than at 25 °C, yet broadly show strength stability across this range, with the pentanary nitride showing the greatest strength loss from 25 °C, to closely match the other equimolar systems in this temperature range. Ductility, through cohesive plasticity, over several percent strain, is now observed, before eventual cracking-induced rapid strength loss. However, the hexanary Al-high system demonstrates approximately 32 % higher σ_y in this range. From 800 to 1000 °C, the best performing system among equimolar compositions is the pentanary high entropy nitride, whilst the heptanary and hexanary Al-low systems show the most rapid decrease of σ_y with temperature. Again, the non-equimolar Al-high system demonstrates 35-42 % higher σ_y in this range than the best performing equimolar system, with $\sigma_y = 6.9 \pm 0.5$ GPa at 1000 °C. Deformation above 900 °C is predominantly cohesive, with local buckling of the upper sections of the pillars or shear plane formation (see TEM below).

It can be seen from the exemplary microcompression loading curves in Fig. 3b, as well as the complete set of material systems and test temperatures in Fig. S10, that there is a noticeable reduction in measured elastic loading modulus, from either 800 or 900 °C depending

on composition, with 1000 °C showing the lowest modulus. This could be associated with chemical reactivity between pillar and punch producing additional interface reaction phases, as well as plastic deformation of the diamond itself, as detailed in Supplementary Note 3. Despite this, we consider the yield points of the loading curves to remain sufficiently distinctive for useful interpretation.

TEM imaging and analysis following microcompression at 1000 °C revealed extensive oxygen inward diffusion in the W-containing, heptanary nitride, see Supplementary Note 4. In the Al-rich hexanary nitride, the spinodally decomposed microstructure is retained as previously in the annealed film, Fig. 4, with a modulation wavelength ~10 nm, and preferential alignment of the Al-rich nano-domains along the film growth direction – i.e. the [001] axis, considering the predominant (002) film texture here. Bending-over of the Al-rich and refractory-metal-rich nano-domains is evident from localized plastic buckling upon compression in the upper half of the pillar (Fig. 4a, b, c), yet the pillar remains dense: no evidence of cracking or boundary decohesion of the columnar grains is seen. Despite the high vacuum environment, multiple oxidation layers surround the Al-high hexanary nitride pillar compressed at 1000 °C: an inner (Ti,V)O_x, an intermediate ZrO_x and finally an outer AlO_x (Fig. S18, Fig. S19). In contrast to the heptanary nitride, the latter outer oxide layer acts as an oxygen diffusion barrier preventing oxygen inward diffusion¹⁹, hence avoiding grain boundary oxide decoration in the pillar bulk.

Discussion

Deformation at room temperature remains brittle for all high entropy nitride systems, but with a higher σ_y : lacking in effective dislocation plasticity as highly directional covalent bonding, the majority constituent of such nitrides²⁰, leads to a high lattice resistance²¹. The high entropy nitrides display initially ductile plasticity from 500 °C, which is consistent with the expectation that thermal activation of bending and turning of interatomic bonds should enable the decline of the lattice resistance (Peierls stress) and activate motion of dislocations in the 0.1-0.3 T_m range¹⁴. All test temperatures are within the latter range considering the melting point of the studied high entropy nitrides can be in the 3200-3400 K²² range if predicted by the rule-of-mixture. Commonly in B1-NaCl structured refractory nitrides, thermalisation of electrons into less localised, less directional metallic states leads to the activation of additional slip systems, now occurring also on the {111}<110>, in addition to {110}<110>, thereby inducing additional ductility^{23,24,25}. The microcompression trends in ductility and σ_y observed here are consistent

with previous high temperature mechanics work²⁶ on simpler B1-NaCl structured multicomponent nitrides, where characterisation was limited to 500 °C – the exact compositions, equimolar or otherwise, not being reported therein, further fruitful comparison is hindered.

Amongst the equimolar compositions, the pentanary system (Ti_{0.23}Hf_{0.15}Nb_{0.17}V_{0.21}Zr_{0.24})N is consistently the strongest system in microcompression up to 1000 °C; strengthening in all equimolar cases is attributable to the lattice resistance of the solid solution – clearly not consistently improved by greater chemical complexity, nor higher melting point nitride formers. The sluggish diffusion characteristic of multi-principle component alloys or high entropy metal sub-lattice nitrides^{27,28}, combined with a relatively low driving force for decomposition, means equimolar systems retain their single-phase structure and, hence, σ_y decrease at high temperatures can be primarily associated with the decline of the lattice resistance and absence of other obstacles for dislocation motion¹⁴. An important feature of the annealing study is that hardness increases in all systems upon annealing above the deposition temperature (450 °C); this is surprising, as commonly hard coatings without an additional microstructural strengthening mechanism would hence lose the strength benefit of a high density of ion-bombardment-induced crystal defects formed during synthesis^{29,30}. As no modification to the 100 nm-scale columnar grain structure upon annealing is evident, we must attribute strengthening to the atomic-scale chemical segregations and re-arrangements observed in Fig. 2a, which may alter local lattice resistance.

The case of the W-containing heptanary nitride is particularly perplexing, as the high performance of the annealing study is not borne out in microcompression. The Tabor factor, that is hardness to yield strength ratio, of 4.6 for the heptanary nitride is indicative of brittleness-limited performance²⁶ – compare to 3.0 and 3.1 of the pentanary and hexanary Al-high nitrides, where cohesive plasticity carries a theoretical Tabor factor of ~ 3 ³¹. It is also important to note the considerably longer thermal holds at each test temperature experienced by the films during microcompression testing: 4 h at least, Fig. S13, compared with 10 min for the annealing study, which justifies oxidation-induced strength loss. Moreover, due to the prolonged time for diffusion in microcompression tests, the ion-bombardment-induced point defects annihilate more efficiently, and the related strengthening efficiently declines starting from 500 °C. Nevertheless, the cause of hardness improvement between annealing at 1000 and 1100 °C remains unclear – only atomic-scale chemical clustering, or short range order, Fig. 2b, is identified here. Such segregation, combined with the high twin boundary density, may be

further exploitable if better understood. The high twin boundary content distinguishes W-containing system from the other equimolar compositions; such faults are uncommon for refractory nitrides due to high stacking fault energies²⁴, and may contribute to the high as-deposited hardness. Since the system contains refractory metal nitrides with low (NbN, VN, and TaN) and high (HfN, TiN, ZrN) stacking fault energies²⁴, the formation of twins in high entropy nitrides can be energetically favoured^{32–34}, especially at higher temperatures³⁵, which can play a hardening role when twin thickness is large^{36,37}. Moreover, any possible departures from ideal randomness, i.e. short-range ordering or clustering, at high annealing temperature can significantly alter the Peierls stress and related strengthening³⁸.

The greatest relative hardness increase is achieved by the hexanary Al-high system (Ti_{0.13}Hf_{0.07}Nb_{0.07}V_{0.10}Zr_{0.12}Al_{0.51})N, which undergoes microstructural decomposition most rapidly – consistent with the higher thermodynamic driving force (Fig. 1a, c) compared with equimolar compositions. The observed XRD peak shoulders, compositional modulation and retention of B1-NaCl structure is consistent with spinodal-type decomposition typical for Al-rich refractory metal-based nitrides^{39,40}. Decomposition of the Al-high solid solution sub-lattice into isostructural (TiHfVNbZr)N- and AlN-rich coherent nano-domains results in spatially fluctuating strain fields between the domains due to the small difference in lattice parameter^{41,42}. These coherency strains can also be accommodated by partial dislocations, stacking faults and misfit dislocation depending of the stage of decomposition^{43,44}. Hence its here-unmatched high temperature strength is provided by coherency strain between decomposed nano-domains⁴⁵, a size-dependent effect, and the associated stacking faults across the domains⁴³, as well as solid solution strengthening of the spinodal phase approximating the pentanary nitride composition. Good ductility is enabled through stacking faults, partial dislocations, and activation of different slip systems, although results here indicate that the pentanary nitride itself presents equally cohesive room temperature plasticity. Additionally, preferential alignment of the spinodal dual-skeleton of percolating phases likely leads to additional strength retention along the growth direction at high temperature⁴⁶. The hexanary 'Al-low' system was also found to decompose through this mechanism after annealing at 1200 °C, but the high temperature strength up to 1000 °C of this system is in the range of all other equimolar systems – likely due to delayed onset of decomposition of the hexanary Al-low compared to the Al-high system, given the lower thermodynamic driving force. Moreover, the high temperature strength of the Al-high system can be explained by a larger amplitude of the composition modulation⁴⁵ compared to the Al-low system (Fig. 2d, f, Fig. S7). The hexanary Al-low system showing the highest hardness after the highest temperature anneal here (Fig. 1d), implying that the transformation

of c-AlN nano-domains into thermodynamically preferred yet softer hexagonal AlN is delayed in the Al-low system in comparison to the Al-high system. Such a trend in the evolution of microstructure and phase composition of Al-low system may provide more optimal strengthening compared to the 'Al-high' condition at temperatures above 1100 °C.

The excellent high temperature strength-ductility combination of the Al-high hexanary system, due to a synergy of several hardening mechanisms accessible upon decomposition of the solid solution via a spinodal mechanism, and sufficient to deform the diamond punch itself, reflects its serious contendership as a next-generation ultrastrong high-temperature ceramics. A simple Tabor factor of 3 predicts a hot hardness of ~20 GPa at 1000 °C. It also highlights the experimental difficulty in investigating such high entropy materials – only B₄C has thus far been suggested as mechanically superior at high temperature⁴⁷, yet it is unlikely to resolve the chemical reactivity issues.

In summary, the current findings show that rather than focusing on equimolar compositions and single-phase formation in high entropy ceramics, the unexplored realm of non-equimolar composition space can offer a pathway to finely tune phase metastability and related complex phase transformation sequences upon metastable phase decomposition to achieve different strengthening mechanisms at high-temperatures. Metastable phase decomposition of the high entropy nitride studied here via a spinodal mechanism produces a chemically modulated microstructure generating coherency strains leading to an ultrahigh yield strength at 1000°C. Future technological developments in such high entropy nitrides may aim to optimize the refractory metal chemistry for greater strength and microstructural stability beyond 1000 °C, whilst retaining the benefits of the early decomposing solid solution bringing spinodally-modulated microstructure and oxidation resistance here, and even exploit additional mechanisms such as high twin densities and atomic-scale chemical segregations and re-arrangements. The strategy of metastability tuning in high entropy nitrides may pave a route towards tailoring their high temperature mechanical properties. We anticipate that a mesmerizing world of ultrastrong high-temperature ceramic materials can be unraveled by delving into the metamorphosis of metastable phases employing, amongst others, spinodal decomposition.

Acknowledgements. AVP acknowledges the financial support from the National Science Centre of Poland (SONATINA 2 project, UMO-2018/28/C/ ST5/00476), the Foundation for Polish Science (FNP) under START scholarship (START 72.2020), and Polish National

Agency for Academic Exchange under the Bekker Programme (PPN/BE K/2019/1/00146/U/00001). AV acknowledges the financial support from the National Science Centre of Poland (SONATINA 2 project, UMO-2018/28/C/ST5/00476). TEJE acknowledges funding from the European Union's Horizon 2020 research and innovation programme under the Marie Skłodowska-Curie grant agreement No. 840222. The contributions of G. Greczynski and B. Bakhit are also gratefully acknowledged.

References

1. Fahrenholtz, W. G. & Hilmas, G. E. Ultra-high temperature ceramics : Materials for extreme environments. *Scr. Mater.* **129**, 94–99 (2017).
2. Xiang, H. *et al.* High-entropy ceramics: Present status, challenges, and a look forward. *Journal of Advanced Ceramics* vol. 10 (2021).
3. Akrami, S., Edalati, P., Fuji, M. & Edalati, K. High-entropy ceramics : Review of principles , production and applications. *Mater. Sci. Eng. R* **146**, 100644 (2021).
4. Oses, C. High-entropy ceramics. *Nat. Rev. Mater.* **5**, 295–309 (2020).
5. Rost, C. M. *et al.* Entropy-stabilized oxides. *Nat. Commun.* **6**, 1–8 (2015).
6. Otto, F., Yang, Y., Bei, H. & George, E. P. Relative effects of enthalpy and entropy on the phase stability of equiatomic high-entropy alloys. *Acta Mater.* **61**, 2628–2638 (2013).
7. Otto, F. *et al.* Decomposition of the single-phase high-entropy alloy CrMnFeCoNi after prolonged anneals at intermediate temperatures. *Acta Mater.* **112**, 40–52 (2016).
8. Kretschmer, A. *et al.* Strain-stabilized Al-containing high-entropy sublattice nitrides. *Acta Mater.* **224**, 117483 (2022).
9. Nayak, G. K., Kretschmer, A., Mayrhofer, P. H. & Holec, D. On correlations between local chemistry, distortions and kinetics in high entropy nitrides: An ab initio study. *Acta Mater.* **255**, 118951 (2023).
10. Johansson, K., Riekehr, L., Fritze, S. & Lewin, E. Multicomponent Hf-Nb-Ti-V-Zr nitride coatings by reactive magnetron sputter deposition. *Surf. Coatings Technol.* **349**, 529–539 (2018).
11. Pshyk, A. V. *et al.* High-entropy transition metal nitride thin films alloyed with Al: Microstructure, phase composition and mechanical properties. *Mater. Des.* **219**, 110798 (2022).
12. Qin, M. *et al.* Dual-phase high-entropy ultra-high temperature ceramics. *J. Eur. Ceram. Soc.* **40**, 5037–5050 (2020).
13. Raabe, D., Li, Z. & Ponge, D. Metastability alloy design. *MRS Bull.* **44**, 266–272 (2019).
14. Wang, J. & Vandeperre, L. J. Deformation and Hardness of UHTCs as a Function of

- Temperature. *Ultra-High Temp. Ceram. Mater. Extrem. Environ. Appl.* **9781118700**, 236–266 (2014).
15. Wang, F., Monteverde, F. & Cui, B. Will high-entropy carbides and borides be enabling materials for extreme environments? *Int. J. Extrem. Manuf.* **5**, (2023).
 16. Kretschmer, A. *et al.* Strain-stabilized Al-containing high-entropy sublattice nitrides. *Acta Mater.* **224**, 117483 (2022).
 17. Mayrhofer, P. H. *et al.* Self-organized nanostructures in the Ti-Al-N system. *Appl. Phys. Lett.* **83**, 2049–2051 (2003).
 18. Pshyk, O. V. *et al.* Discovery of Guinier-Preston zone hardening in refractory nitride ceramics. *Acta Mater.* **255**, (2023).
 19. Greczynski, G., Hultman, L. & Odén, M. X-ray photoelectron spectroscopy studies of Ti_{1-x}Al_xN (0 ≤ x ≤ 0.83) high-temperature oxidation: The crucial role of Al concentration. *Surf. Coatings Technol.* **374**, 923–934 (2019).
 20. *Comprehensive Materials Processing*. (Elsevier, 2014). doi:10.1007/s13398-014-0173-7.2.
 21. *Materials Science of Carbides, Nitrides and Borides*. (Springer Science+Business Media, 1999). doi:https://doi.org/10.1007/978-94-011-4562-6.
 22. *The Chemistry of Transition Metal Carbides and Nitrides*. (Blackie Academic & Professional, 1996).
 23. Hannink, R. H. J., Kohlstedt, D. L. & Murray, M. J. Slip System Determination in Cubic Carbides by Hardness Anisotropy. *Proc. R. Soc. A* **326**, 409–420 (1972).
 24. Yu, H., Bahadori, M., Thompson, G. B. & Weinberger, C. R. Understanding dislocation slip in stoichiometric rocksalt transition metal carbides and nitrides. *J. Mater. Sci.* **52**, 6235–6248 (2017).
 25. Csanádi, T., Castle, E., Reece, M. J. & Dusza, J. Strength enhancement and slip behaviour of high-entropy carbide grains during micro-compression. *Sci. Rep.* 1–14 (2019) doi:10.1038/s41598-019-46614-w.
 26. Wheeler, J. M., Raghavan, R., Chawla, V., Morstein, M. & Michler, J. Deformation of Hard Coatings at Elevated Temperatures. *Surf. Coat. Technol.* **254**, 382–387 (2014).
 27. Kirnbauer, A. *et al.* Mechanical properties and thermal stability of reactively sputtered multi-principal-metal Hf-Ta-Ti-V-Zr nitrides. *Surf. Coatings Technol.* **389**, 125674 (2020).
 28. Kretschmer, A. *et al.* Improving phase stability, hardness, and oxidation resistance of reactively magnetron sputtered (Al,Cr,Nb,tai,Ti)N thin films by Si-alloying. *Surf. Coatings Technol.* **416**, 127162 (2021).
 29. Schaffer, J. P., Perry, A. J. & Brunner, J. Defects in hard coatings studied by positron annihilation spectroscopy and x-ray diffraction. *J. Vac. Sci. Technol. A Vacuum, Surfaces, Film.* **10**, 193–207 (1992).
 30. Zhang, Z. *et al.* Correlating point defects with mechanical properties in nanocrystalline TiN thin films. *Mater. Des.* **207**, 109844 (2021).

31. Vandeperre, L. J., Giuliani, F. & Clegg, W. J. Effect of elastic surface deformation on the relation between hardness and yield strength. *J. Mater. Res.* **19**, 3704–3714 (2004).
32. Huang, H., Shao, L. & Liu, H. Stacking fault energies of high-entropy nitrides from first-principles calculations. *Solid State Commun.* **327**, 114210 (2021).
33. Joelsson, T., Hultman, L. & Hugosson, H. W. Phase stability tuning in the Nb x Zr 1 – x N thin-film system for large stacking fault density and enhanced mechanical strength. **131922**, 10–13 (2011).
34. Hugosson, H. W., Jansson, U., Johansson, B. & Eriksson, O. Restricting dislocation movement in transition metal carbides by phase stability tuning. *Science (80-.)*. **293**, 2434–2437 (2001).
35. Xu, Z. *et al.* Insight into the structural evolution during TiN film growth via atomic resolution TEM. *J. Alloys Compd.* **754**, 257–267 (2018).
36. Liu, P., Xie, J., Wang, A., Ma, D. & Mao, Z. Molecular dynamics simulation on the deformation mechanism of monocrystalline and nano-twinned TiN under nanoindentation. *Mater. Chem. Phys.* **252**, 123263 (2020).
37. Fu, T. *et al.* In-plane anisotropy and twin boundary effects in vanadium nitride under nanoindentation. *Sci. Rep.* **7**, 1–9 (2017).
38. Wang, Y., Csanádi, T., Zhang, H., Dusza, J. & Reece, M. J. Enhanced Hardness in High-Entropy Carbides through Atomic Randomness. *Adv. Theory Simulations* **2000111**, 1–8 (2020).
39. Mikula, M. *et al.* Thermally induced age hardening in tough Ta-Al-N coatings via spinodal decomposition. *J. Appl. Phys.* **121**, 155304 (2017).
40. Hao, J. *et al.* Spinodal decomposition in the Ta-Mo-Al-N films activated by Mo incorporation : Toward enhanced hardness and toughness. **44**, 21358–21364 (2018).
41. Tasnádi, F. *et al.* Significant elastic anisotropy in Ti_{1-x}Al_xN alloys. *Appl. Phys. Lett.* **97**, 23–26 (2010).
42. Cahn, J. Hardening by spinodal decomposition. *Acta Metall.* **11**, 1275–1282 (1963).
43. Salamaña, J. *et al.* High-resolution STEM investigation of the role of dislocations during decomposition of Ti_{1-x}Al_xN_y. *Scr. Mater.* **229**, 115366 (2023).
44. Rafaja, D. *et al.* Crystallography of phase transitions in metastable titanium aluminium nitride nanocomposites. *Surf. Coatings Technol.* **257**, 26–37 (2014).
45. Kato, M., Mori, T. & Schwartz, L. H. Hardening by spinodal modulated structure. *Acta Metall.* **28**, 285–290 (1980).
46. Amberger, D., Eisenlohr, P. & Göken, M. On the importance of a connected hard-phase skeleton for the creep resistance of Mg alloys. *Acta Mater.* **60**, 2277–2289 (2012).
47. Wheeler, J. M. & Michler, J. Invited article: Indenter materials for high temperature nanoindentation. *Rev. Sci. Instrum.* **84**, 1–11 (2013).

Figures

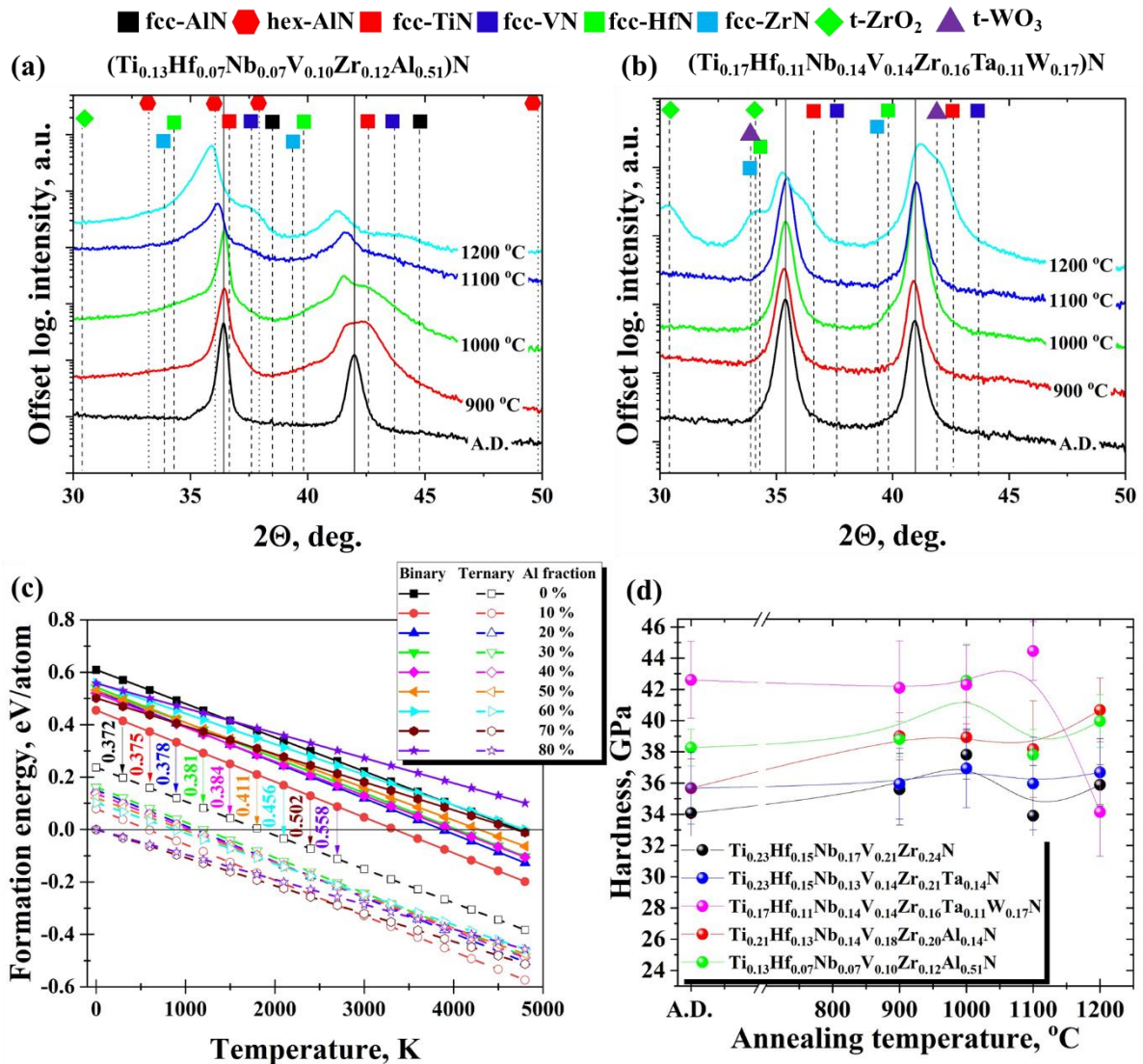


Fig. 1. (a-b) XRD patterns for hexanary 'Al-high' ($\text{Ti}_{0.13}\text{Hf}_{0.07}\text{Nb}_{0.07}\text{V}_{0.10}\text{Zr}_{0.12}\text{Al}_{0.51}\text{N}$) and heptanary ($\text{Ti}_{0.17}\text{Hf}_{0.11}\text{Nb}_{0.14}\text{V}_{0.14}\text{Zr}_{0.16}\text{Ta}_{0.11}\text{W}_{0.17}\text{N}$) thin films before and after annealing in vacuum at 900, 1000, 1100, 1200. (c) Calculated formation energies, E_f , of B1-NaCl pentanary system and hexanary system with different Al fraction as a function of temperature. E_f for systems with metal ratios on the cation sublattice similar to experimental samples is calculated considering binary (solid lines, full symbols) or ternary (dashed line, empty symbols) decomposition products, and the decomposition potential, i.e. driving force for decomposition, is determined as the energy difference between these energies (arrows with captions show the difference for each composition in eV). The thermodynamic driving force for decomposition becomes more positive with the increase of Al content in the solid solution. The latter implies that the solid solutions with higher Al content possess the highest driving force for the decomposition into less complex phases or solid solutions even at high temperatures. (d) Nanoindentation hardness of all films performed before and after annealing in vacuum at different temperatures in the range 900-1200 °C.

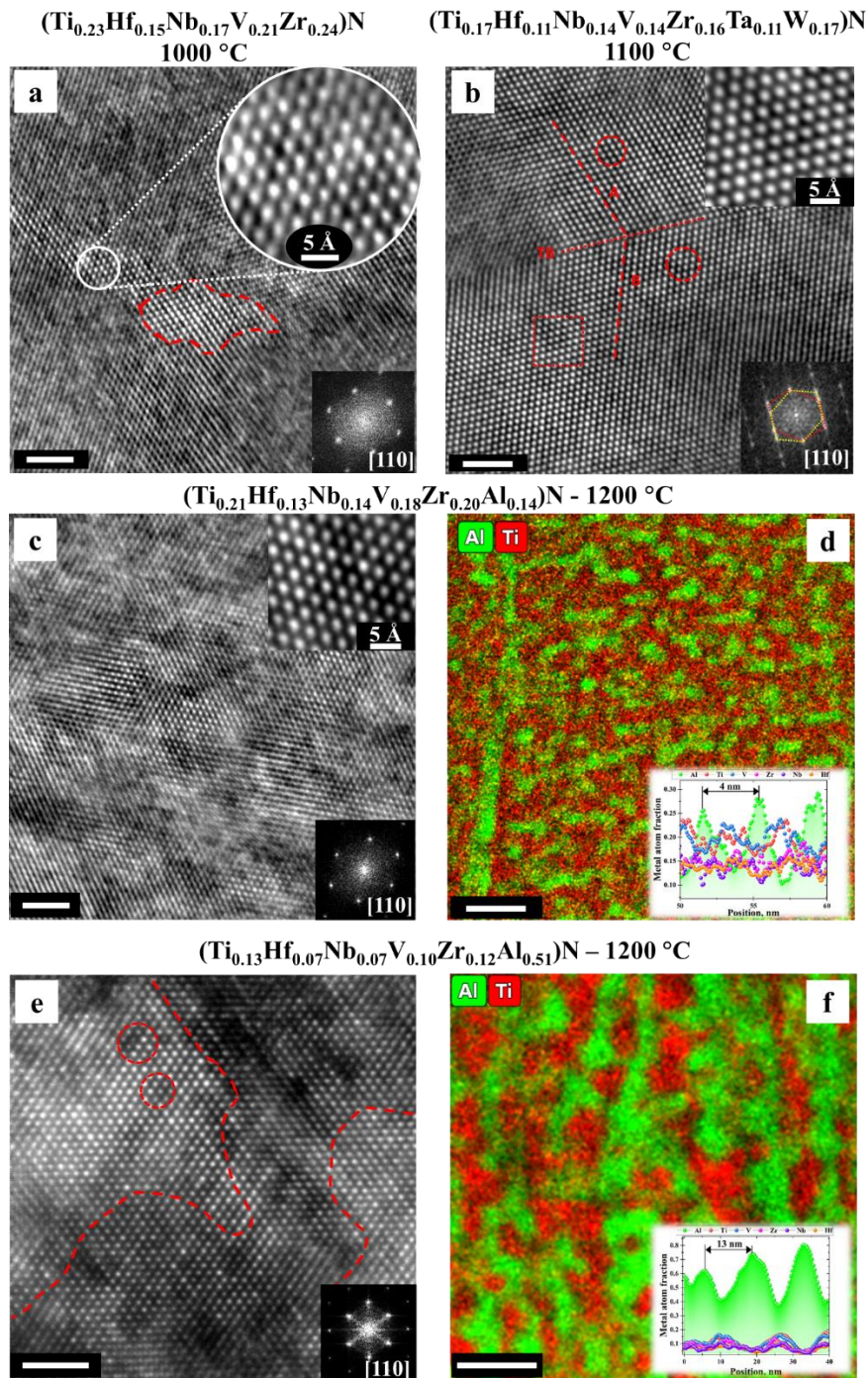


Fig. 2. (a) Cross-sectional STEM-HAADF acquired along [110] zone axis from pentanary nitride annealed at 1000 °C and (b) heptanary nitride annealed at 1100 °C. Cross-sectional STEM-HAADF images taken along [110] zone axis and STEM-EDX color-coded combined maps of Ti-Al acquired from (c, d) the hexanary 'Al-low' and (e, f) hexanary 'Al-high' films after annealing at 1200 °C. Red dashed lines show the borders of the high Z areas, red dashed circles mark the local chemical segregation across the metal sublattice enlarged in the upper right insets in (a), (b) and (c). Fast Fourier transform (FFT) patterns of (a), (b), (c) and (e) are presented in bottom right inserts. Scale bars in (a) – (c) and (e) are 2 nm; in (d) it is 10 nm and in (f) – 20 nm.

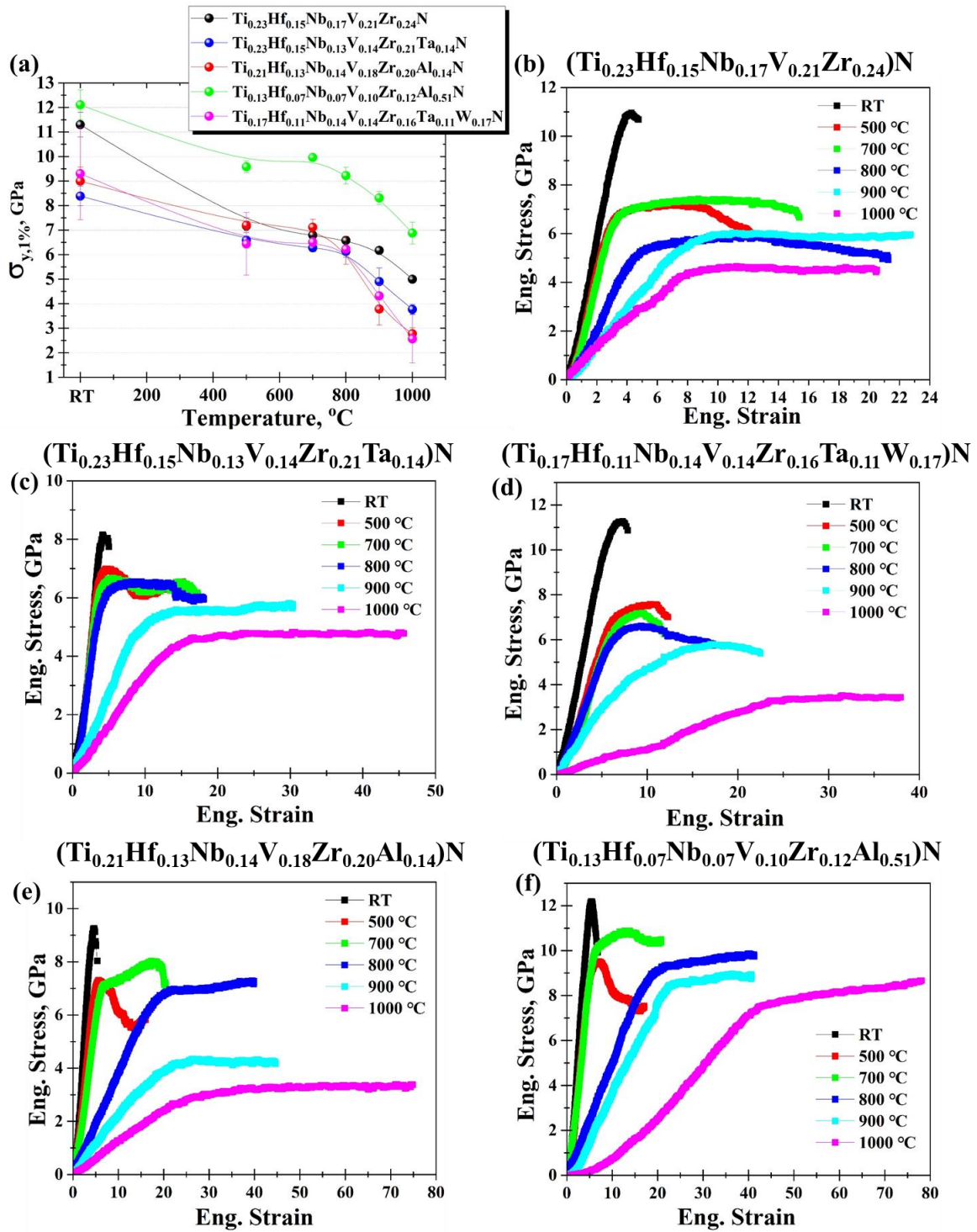


Fig. 3. (a) Yield strength at 1 % strain and corresponding representative stress-strain curves for (b) (TiHfNbVZr)N, (c) hexanary (TiHfNbVZrTa)N, and (d) heptanary (TiHfNbVZrTaW)N, (e) the hexanary Al-low and (f) Al-high pillars compressed at RT, 500 °C, 700 °C, 800 °C, 900 °C, and 1000 °C. For a statistical accuracy at least 4-5 pillars are compressed for each film composition at each test temperature.

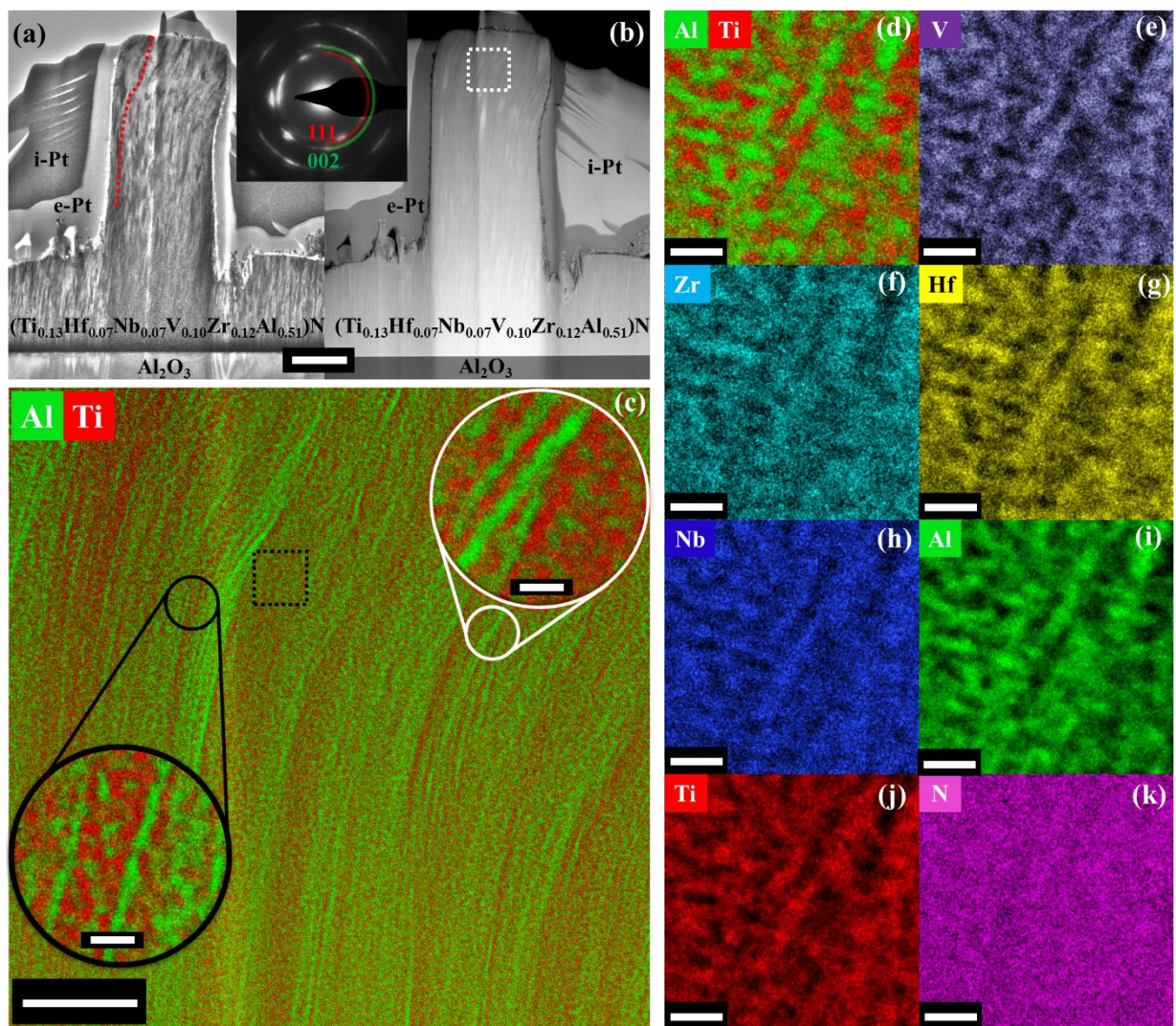


Fig. 4. Overview cross-sectional (a) BF-TEM (red dotted line serves as a guide to buckling of the columnar grains) and (b) Z-contrast STEM images from the hexanary Al-high pillar after compression at 1000 °C with corresponding SAED pattern as an inset, and electron and ion-deposited Pt protective straps (e-Pt & i-Pt, respect.) indicated. (c) EDX color-coded maps of Al and Ti acquired from the white square in (b) with insets demonstrating EDS maps with a higher magnification. EDS color-coded maps of (d) Ti-Al, (e) V, (f) Zr, (g) Hf, (h) Nb, (i) Al, (j) Ti, and (k) N. Scale bar in (a) and (b) is 1 μm , in (c) it is 200 nm (20 nm in the insets), and in (d) – (k) they are 20 nm.

Supplementary Material

Methods

Refractory-metal-based pentanary (TiHfNbVZr)N, hexanary (TiHfNbVZrTa)N, and heptanary (TiHfNbVZrTaW)N thin films are grown by direct current (DC) magnetron sputtering in an industrial CemeCon AG CC800/9 magnetron sputtering system. The hexanary Al-low and Al-rich (TiHfNbVZrAl)N are grown by a hybrid high-power impulse and DC magnetron co-sputtering HiPIMS/DCMS, see previous publication for details¹. The films are grown with 6 μm thickness on (0001) single crystalline sapphire substrates.

The micro-pillars are produced with the equivalent diameter of $\sim 1.8 \mu\text{m}$ and the final taper angle not exceeding 3° by focused ion beam (FIB) milling in a Tescan Lyra 3 instrument. The micro-pillars are milled with heights of $\sim 4\text{-}4.5 \mu\text{m}$ in order to avoid sample/pillar penetration into the substrate during compression, and to avoid pillar-on-pedestal effects.

Micro-pillar compression is performed *in situ* in a Zeiss DSM 962 scanning electron microscope (SEM, base pressure 1.3×10^{-3} Pa) using an Alemnis SEM indenter extensively modified for operation at temperatures up to $1000 \text{ }^\circ\text{C}$, with pyrolytic graphite-on-pyrolytic boron nitride heaters to achieve independent heating of both sample and indenter². The compression is performed by means of a $5 \mu\text{m}$ diameter diamond flat punch manufactured for high-temperature experiments by Synton-MDP. To minimize the effect of thermal drift during compression at elevated temperatures, the matching of the sample temperature and indenter temperature follows the procedure described elsewhere², to ensure thermal equilibrium at contact, considering the impact of substantial mutual radiative heating above $\sim 600 \text{ }^\circ\text{C}$ ³. Initial calibration of the tip temperature is achieved by indentation of the molybdenum holder adjacent to a spot welded reference thermocouple. The calibration of the compliance of the loading frame is performed at test temperatures by indentation of the (0001) single crystalline sapphire substrate material using a diamond Berkovich indenter, according to the method in⁴. In order to achieve stabilization of the system at high temperatures, the heating rate is set to $5 \text{ }^\circ\text{C}/\text{min}$ and the holding time for complete equilibration of tip/sample temperature, and the rest of the loading frame and sensors, before tests is $\sim 4\text{-}5$ hours at each test temperature – see Supplementary Fig. S? for an exemplary heating schedule. For statistical accuracy at least 4-5 pillars are compressed for each film composition at each test temperature. The compression is conducted at room temperature (RT), $500 \text{ }^\circ\text{C}$, $700 \text{ }^\circ\text{C}$, $800 \text{ }^\circ\text{C}$, $900 \text{ }^\circ\text{C}$ and $1000 \text{ }^\circ\text{C}$, once the isothermal conditions for the sample and punch are achieved. The micro-pillars are compressed

in displacement control mode with a strain rate of $1 \times 10^{-3} \text{ s}^{-1}$ at temperatures from RT to 900 °C, and with a strain rate of $1 \times 10^{-2} \text{ s}^{-1}$ at 1000 °C, for practical reasons. The temperature-dependent compliance of the sapphire substrate^{5,6}, and the pillar geometry, is taken into account by applying Sneddon's and Zhang's corrections⁷ during yield strength calculations using the associated MicroMechanics Data Analyser (MMDA) software.

Film and micro-pillar cross-sectional lift-out for scanning and transmission electron microscopy (STEM) and selected area electron diffraction (SAED) is performed by FIB in a FEI Helios NanoLab G3 UC Dual Beam SEM/Ga⁺ FIB system. TEM investigations are performed using a probe-corrected Thermo Fisher Scientific Titan Themis 200 G3 operated at 200 kV. Energy dispersive X-ray spectroscopy (EDX) is acquired with the integrated SuperX detector. The annealing is performed in vacuum with the heating rate of 10 °C/min to the annealing temperature T_a , which is in the range 900-1200 °C, and then kept at T_a for 10 min. Following anneals, the furnace is allowed to naturally cool to room temperature. The phase composition of the films before and after annealing is determined using Bragg-Brentano X-ray diffraction (XRD) using a PANalytical Empyrean X-ray diffractometer.

Nanoindentation hardness, H , is measured using a Vantage Alpha Nanotester (Micromaterials Ltd., UK) equipped with a Berkovich tip. Indentations are performed with a constant load of 30 mN with a dwell period of 5 s, resulting in indentation depths <10 % of the total film thickness allowing for minimizing effect of the substrate on the measured hardness. Hardness is calculated following the Oliver and Pharr method⁴ while the standard deviation errors are extracted from 25 indents (separated by 40 μm in square grids).

Ab initio DFT calculations are performed following the methodology described elsewhere^{8,9}

Supplementary Notes

Supplementary Note 1

Many studies focus on maximizing configurational entropy (using equimolar ratios of elements) for greater single phase stabilization^{10,11} of high-entropy ceramic materials; differing combinations and increasing the number of elements has achieved properties often highly surpassing those of the constituent conventional ceramic components^{11,12}.

Although some ceramic system demonstrate high-temperature stability^{13,14}, recent theoretical studies has shown that all 126 equimolar high-entropy nitrides studied in¹⁵ are metastable with respect to all corresponding equimolar lower-entropy nitride phases that was

confirmed experimentally that additionally confirms the studies of other authors¹⁶. Therefore, exploiting the metastability of high-entropy ceramics can offer additional phase space and thus multiple advantages for tuning beneficial properties.

Supplementary Note 2

The local lattice disorder inherent in high-entropy ceramics arising from many different sized and chemically distinct elements and fluctuations in the local chemical environment has an influence on the movement of diffusing species, defects and dislocations^{17,18}. Therefore, the high-entropy concept provides ample room for further well-targeted improvement of high-temperature mechanical properties¹⁹. While mechanical properties are enhanced by severe lattice distortion (solid-solution strengthening), nanograin microstructure impeding dislocation motion (Hall-Petch strengthening), and by changes in and/or elimination of lattice slip systems²⁰, the inhibition of grain coarsening typical for high entropy ceramics at elevated temperatures allows to retain mechanical properties¹⁴. Theoretical calculations demonstrate that high entropy ceramics show a slow reduction in tensile and shear strength with temperature²¹. Although only few studies report about mechanical behavior of high entropy ceramics at elevated temperatures^{19,22,23}, they clearly demonstrate exceptional potential of high entropy ceramics to become new high-temperature materials²⁴. However, most rare reports in the literature deal with *post mortem* mechanical characterization of high entropy ceramics and their high-temperature mechanical properties under real operating conditions are still lacking detailed characterizations^{18,25,26}. The possible reason of the latter is that most of high-entropy ceramics are synthesized in thin film form. Owing to highly non-equilibrium conditions, physical vapour deposition (PVD) is typically the most preferential method for metastable high-entropy ceramic synthesis. Characterization of mechanical properties of thin films at high temperatures has been not feasible due to the limited volume available and related obstacles. However, recent advancements in thermomechanical testing methods for micro/nano-scale materials allow to overcome the critical challenges associated with temperature control during material characterization, specimen size and resolution of measurements²⁷.

Supplementary Note 3

In Fig. S10, the low elastic loading modulus measured from either 800 or 900 °C, depending on composition, is arrowed; the lowest modulus is consistently associated with testing at 1000 °C. This measured low modulus is despite the presented data have undergone sensor drift corrections, temperature-dependent loading frame modulus correction, Fig. S15,

and sink-in correction accounting for the minor (~10%) thermal reduction in elastic modulus of the (0001) sapphire substrate by 1000 °C. Initial suspicion of plastic deformation of the sapphire substrate at high temperature was proven incorrect: a cross-sectional liftout of a hexanary Al-high pillar compressed at 1000 °C imaged by TEM reveals no deviation of the film-substrate interface, nor evidence of remaining crystal defects in the sapphire (dislocations or twins), Fig. 4b. According to previous studies, fracture of sapphire at this temperature is preceded by deformation twinning⁵; hence as neither occur here, this indicates that load applied to the micropillar is effectively distributed in the ~2 μm film thickness below the pillars.

To elucidate this phenomenon further, TEM analysis of a central cross-section of the diamond punch itself was carried out – indeed immediately from SEM imaging, it is evident that imprints of the tops of the micropillars are left in the punch surface after testing up to 1000 °C, Fig. S11. Extensive chemical reactivity between punch and high entropy refractory nitride pillars was observed, resulting in consumption of the punch and the formation of mechanically weaker oxide phases²⁸, as well as carbides, oxy-carbides and a carbo-nitride several hundred nanometres thick in total, Fig. S12. Specifically, we identify on the punch surface: AlO_x particles, (Zr,Hf)O_x particles, CN_x particles, a thin TiC_x layer, a thick (Ti,Zr,Hf,V,Nb,Ta,Al,Si)O_xC_y layer interfacing the diamond, and a SiO_x outer layer, where the provenance of Si content is a separate Si-doped refractory high entropy nitride series.

In addition, evidence of mechanical deformation of the diamond (stacking faults, on at least 4 distinct systems, as well as an elevated density of ordinary dislocations) was found after testing up to 1000 °C, Fig. S11; these faults are most dense near the contact interface between pillar and punch. Although this is not definitive proof of plasticity generated at high temperature – rather than initially present from punch production, or related to low temperature testing – it is nevertheless consistent in both crystal deformation mechanism, and applied stress (7.9 GPa, vs. ~8.5 GPa maximum here) with previous reports of plasticity in 3.5 GPa anvil-confined 5 μm diamond powder²⁹.

Both the chemical reactivity and mechanical deformation of the diamond punch are expected to have occurred most readily at the highest test temperatures, according to straightforward kinetic arguments, and provide pathways for additional punch displacement to be achieved by a given load in those test conditions.

Supplementary Note 4

W-containing, heptanary nitride: TEM imaging and analysis following micro-compression at 1000 °C revealed extensive oxygen inward diffusion, Fig. S16, manifested as a

high oxygen content along columnar grain boundaries in the upper third of the film, Fig. S17, and a ladder-like structure within the grains there, with the horizontal oxygen-rich rungs coincident with locally heightened Hf and Zr contents. Diffraction from the low volume of these additional phases was not captured in the SAED of the upper half of the film. Grain-scale segregation of W remains, along with atom-scale segregations.

Supplementary Tables

Table S1. Elemental composition of the samples derived from the combined measurements by means of XPS and ToF-ERDA.

Sample	Composition (at.%)											
	N	Al	Ti	Hf	V	Zr	Nb	Ta	W	Ar	O	C
(TiVZrNbHf)N	48.2	–	11.8	7.6	10.5	12.2	7.8	–	–	0.4	0.8	0.7
(TiVZrNbHf) _{0.86} Al _{0.14} N	48	6.9	10.3	6.5	9	10.2	6.8	–	–	0.4	1	0.8
(TiVZrNbHf) _{0.49} Al _{0.51} N	48.8	25.1	11.8	7.6	5.1	5.8	3.5	–	–	0.4	0	0.7
(TiVZrNbHfTa)N	48.2	–	11.5	7.6	6.9	10.4	6.5	6.7	–	0.5	0.9	0.8
(TiVZrNbHfTaW)N	45.0	–	9.7	5.6	7.3	9.5	5.9	5.6	9.6	0.5	0.6	0.9

Supplementary Figures

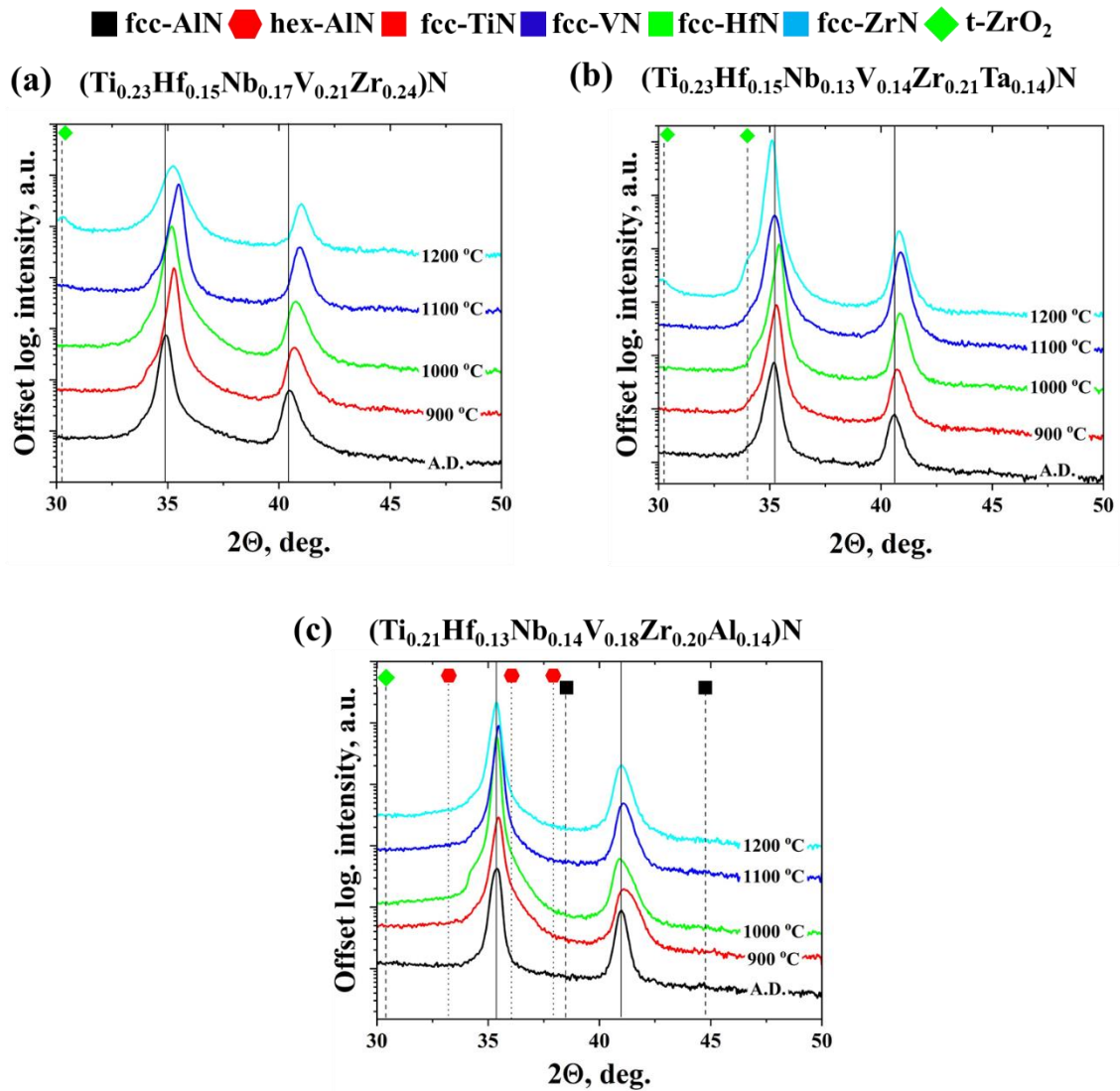
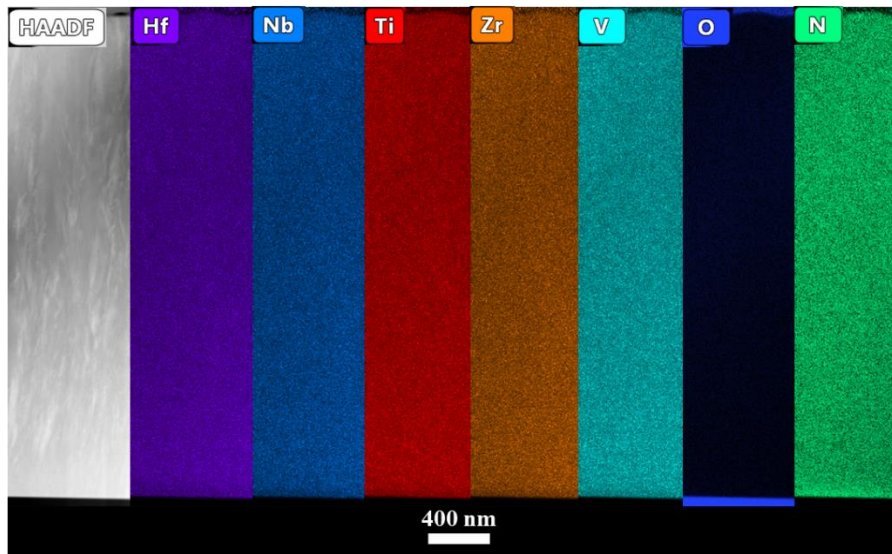


Fig. S1. (a-c) XRD patterns for pentanary (Ti_{0.23}Hf_{0.15}Nb_{0.17}V_{0.21}Zr_{0.24})N, hexanary (Ti_{0.23}Hf_{0.15}Nb_{0.13}V_{0.14}Zr_{0.21}Ta_{0.14})N, and hexanary 'Al-low' (Ti_{0.21}Hf_{0.13}Nb_{0.14}V_{0.18}Zr_{0.20}Al_{0.14})N thin films before and after annealing in vacuum at 900, 1000, 1100, and 1200 °C.

(a) $(\text{Ti}_{0.23}\text{Hf}_{0.15}\text{Nb}_{0.17}\text{V}_{0.21}\text{Zr}_{0.24})\text{N}$ - 1000 °C



(b) $(\text{Ti}_{0.17}\text{Hf}_{0.11}\text{Nb}_{0.14}\text{V}_{0.14}\text{Zr}_{0.16}\text{Ta}_{0.11}\text{W}_{0.17})\text{N}$ - 1100 °C

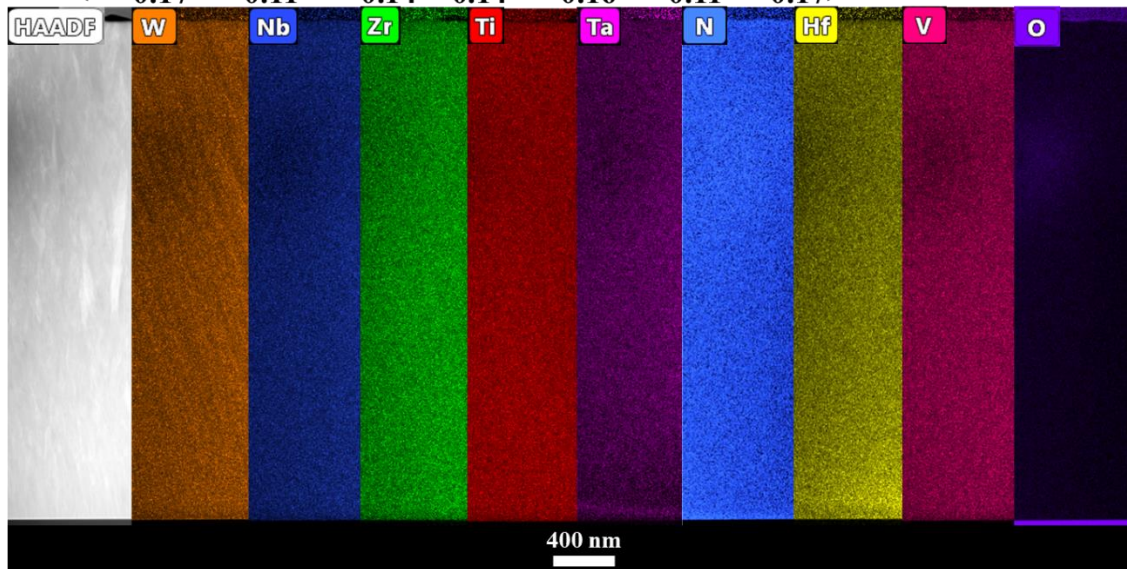


Fig. S2. EDX color-coded elemental maps acquired from (a) pentanary nitride annealed at 1000 °C and (b) heptanary nitride annealed at 1100 °C.

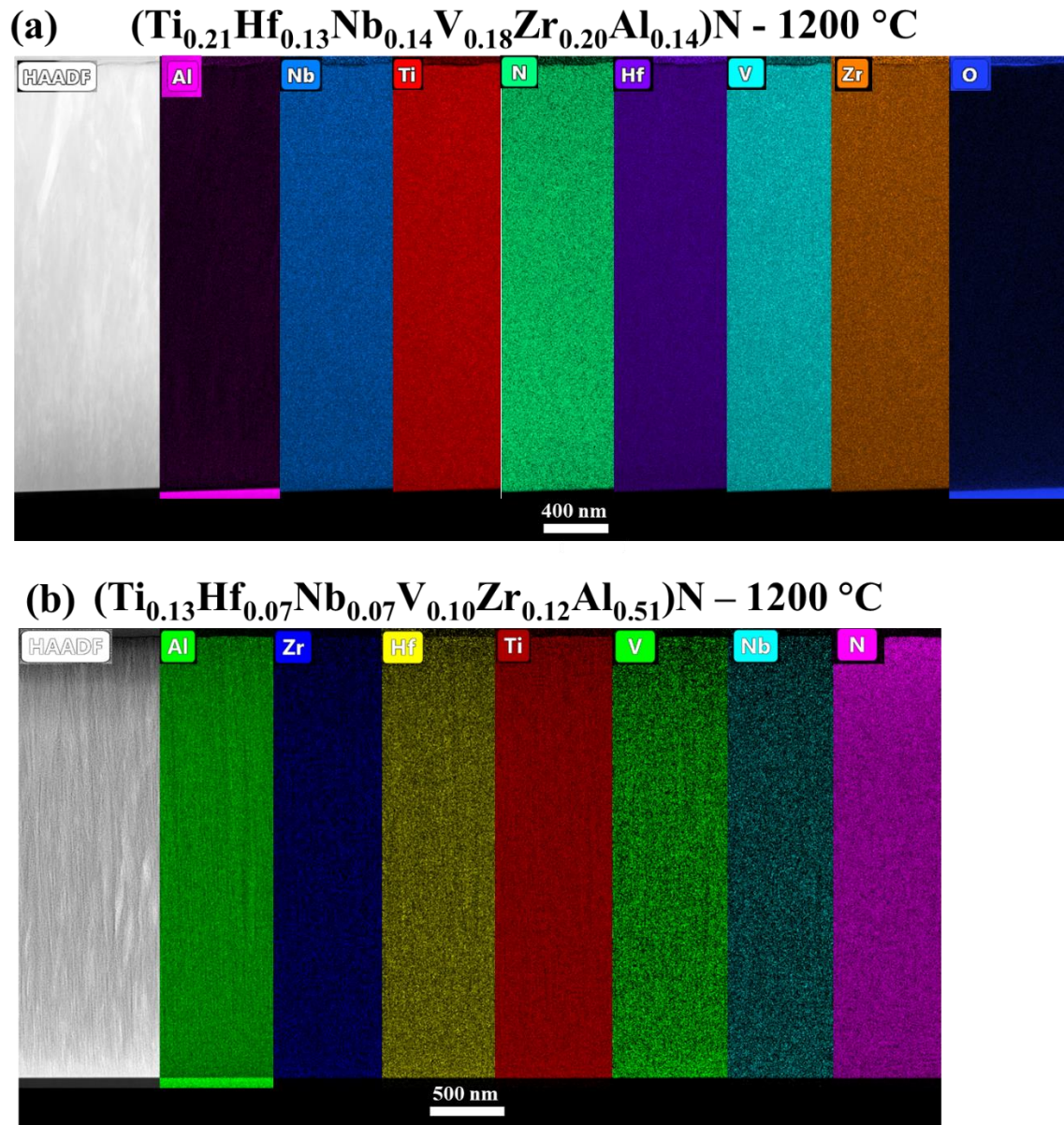


Fig. S3. EDX color-coded elemental maps acquired from (a) the hexanary 'Al-low' $(\text{Ti}_{0.21}\text{Hf}_{0.13}\text{Nb}_{0.14}\text{V}_{0.18}\text{Zr}_{0.20}\text{Al}_{0.14})\text{N}$ and (b) hexanary 'Al-high' $(\text{Ti}_{0.13}\text{Hf}_{0.07}\text{Nb}_{0.07}\text{V}_{0.10}\text{Zr}_{0.12}\text{Al}_{0.51})\text{N}$ films after annealing at $1200\text{ }^\circ\text{C}$.

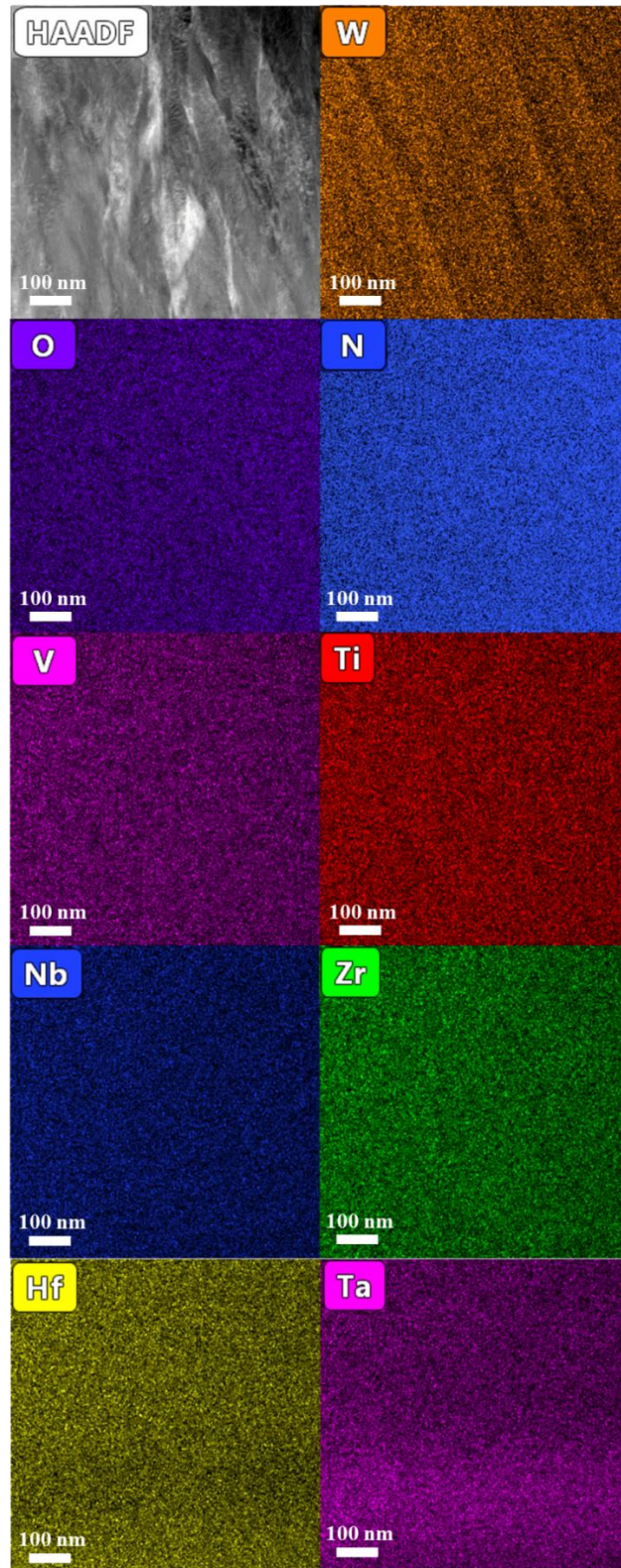
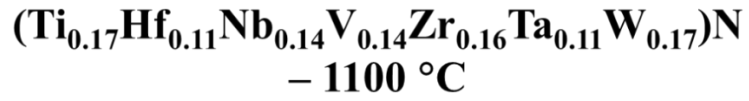


Fig. S4 Magnified EDX color-coded elemental maps acquired from heptanary nitride annealed at 1100 °C.

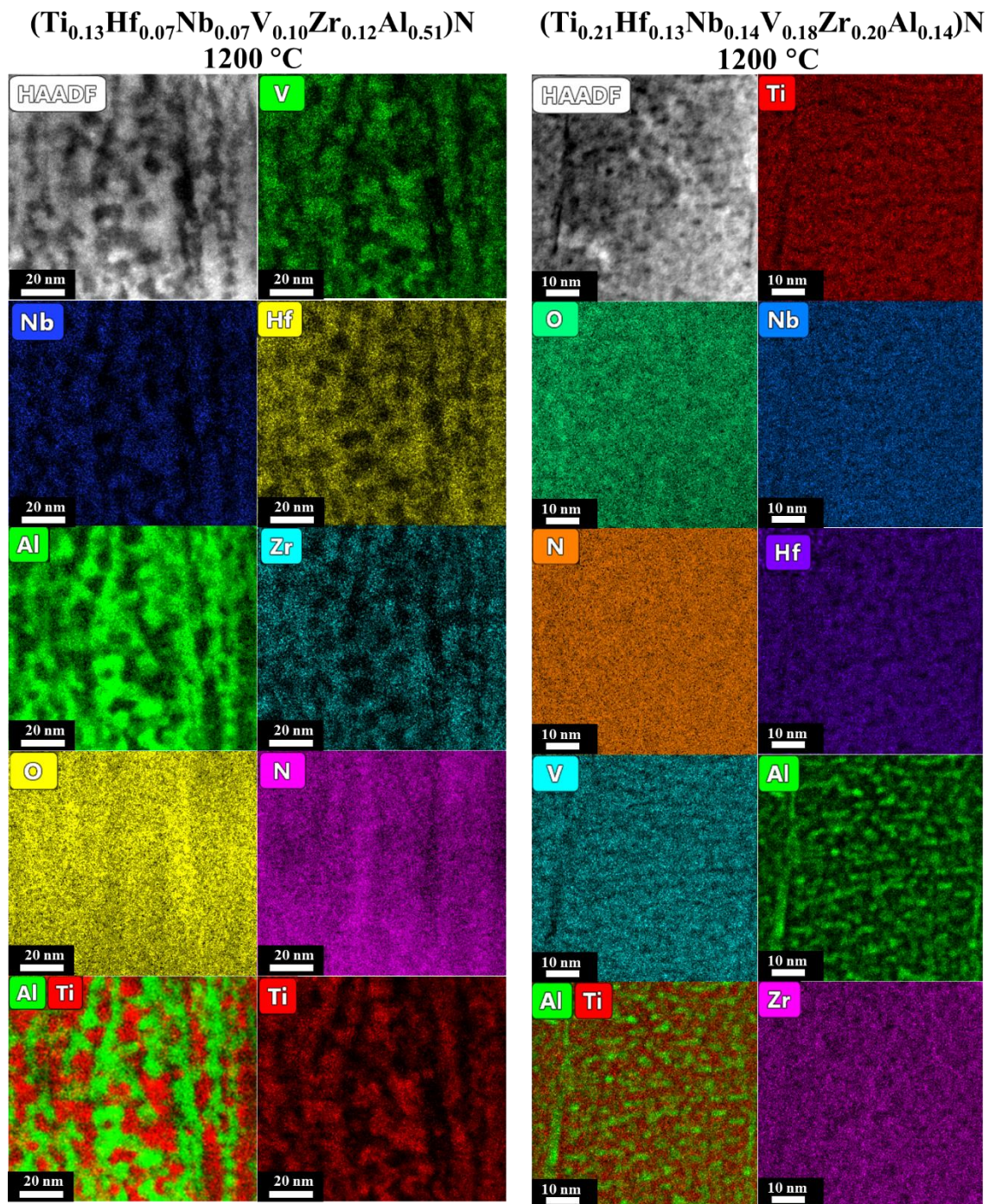


Fig. S5 Magnified EDX color-coded elemental maps acquired from the hexanary 'Al-high' $(\text{Ti}_{0.13}\text{Hf}_{0.07}\text{Nb}_{0.07}\text{V}_{0.10}\text{Zr}_{0.12}\text{Al}_{0.51})\text{N}$ and the hexanary 'Al-low' $(\text{Ti}_{0.21}\text{Hf}_{0.13}\text{Nb}_{0.14}\text{V}_{0.18}\text{Zr}_{0.20}\text{Al}_{0.14})\text{N}$ films after annealing at 1200 °C.

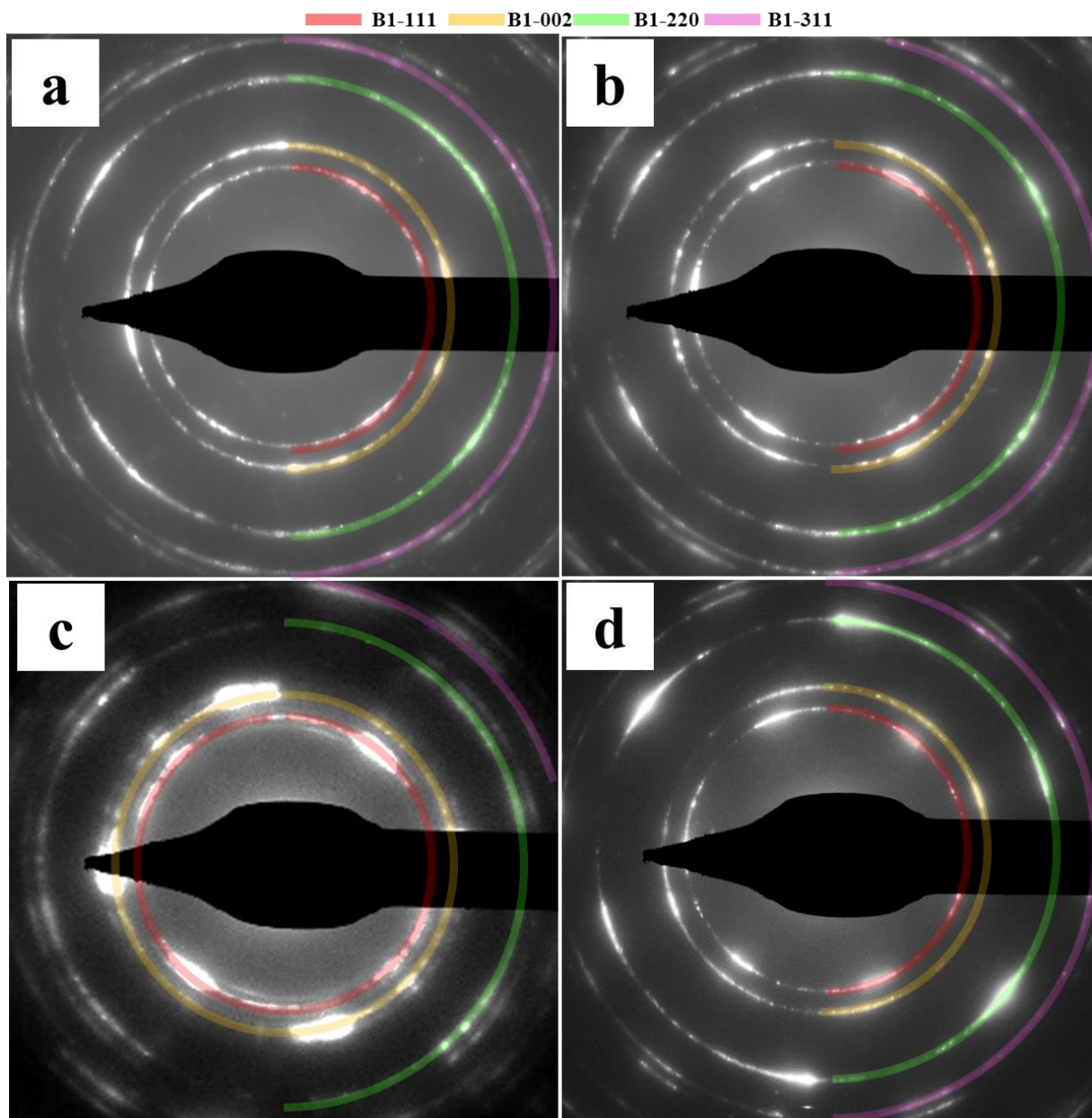


Fig. S6. SAED acquired from (a) heptanary nitride annealed at 1100 °C, (b) pentanary nitride annealed at 1000 °C, (c) hexanary 'Al-high' and (d) hexanary 'Al-low' films after annealing at 1200 °C. Film growth direction is horizontal for the SAEDs presented here.

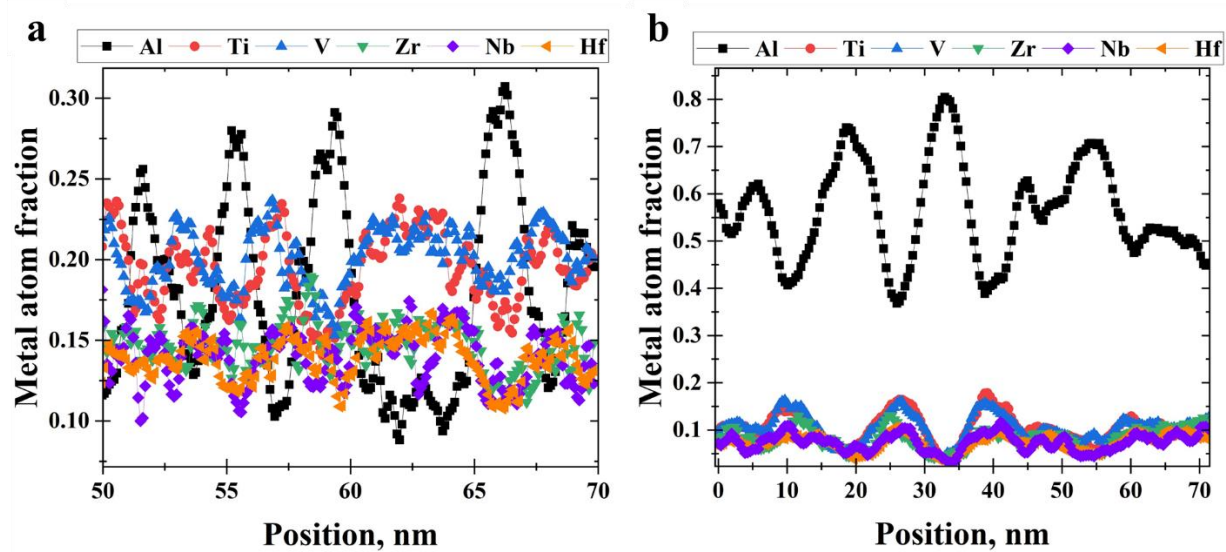


Fig. S7. EDS line scans acquired from (a) hexanary 'Al-low' and (b) hexanary 'Al-high' films after annealing at 1200 °C.

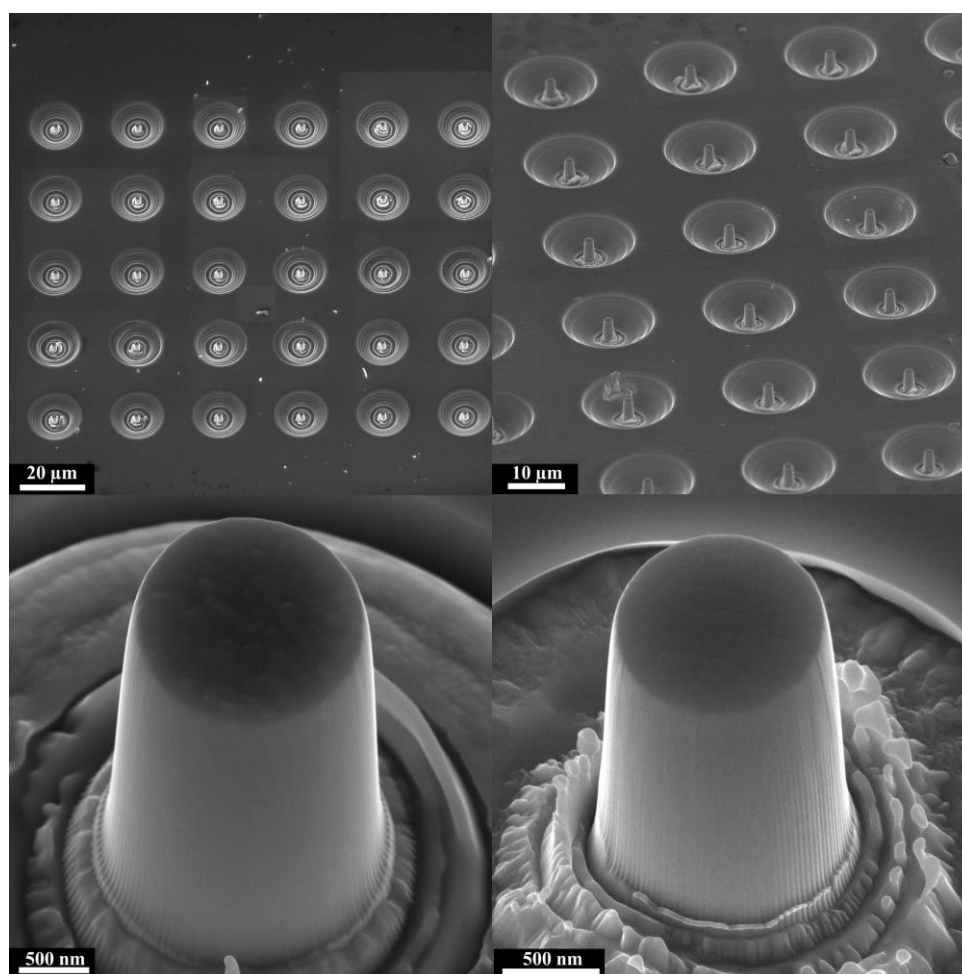


Fig. S8. SEM images of representative sets of FIB-milled micro-pillars before microcompression, viewed at 45° tilt angle.

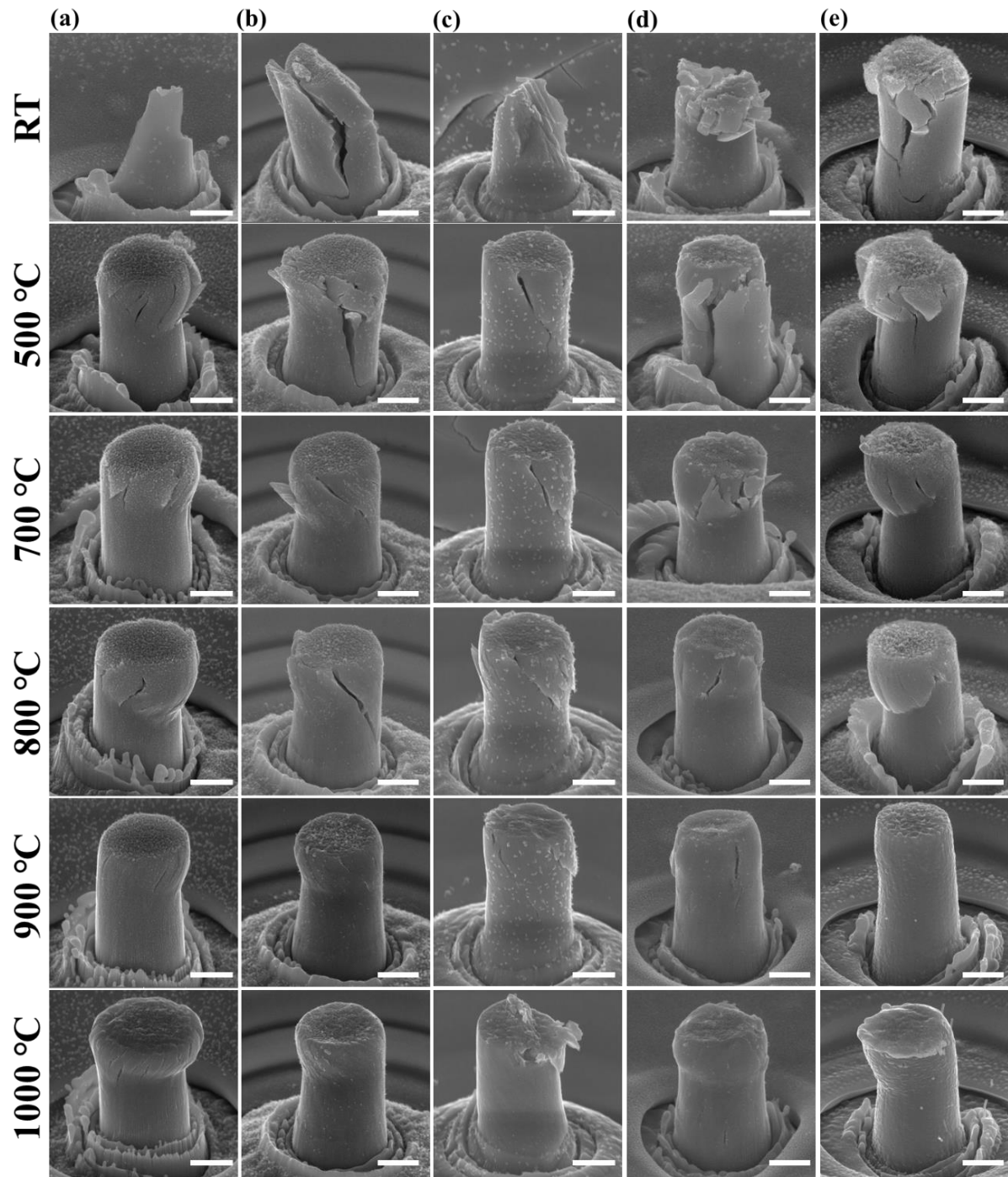


Fig. S9. SEM images of micro-pillars deformation and fracture for pentanary (a) (TiHfNbVZr)N, (b) hexanary (TiHfNbVZrTa)N, (c) heptanary (TiHfNbVZrTaW)N, (d) the hexanary Al-low and (e) Al-high (TiHfNbVZrAl)N systems after compression at room temperature (RT), 500 °C, 700 °C, 800 °C, 900 °C, and 1000 °C.

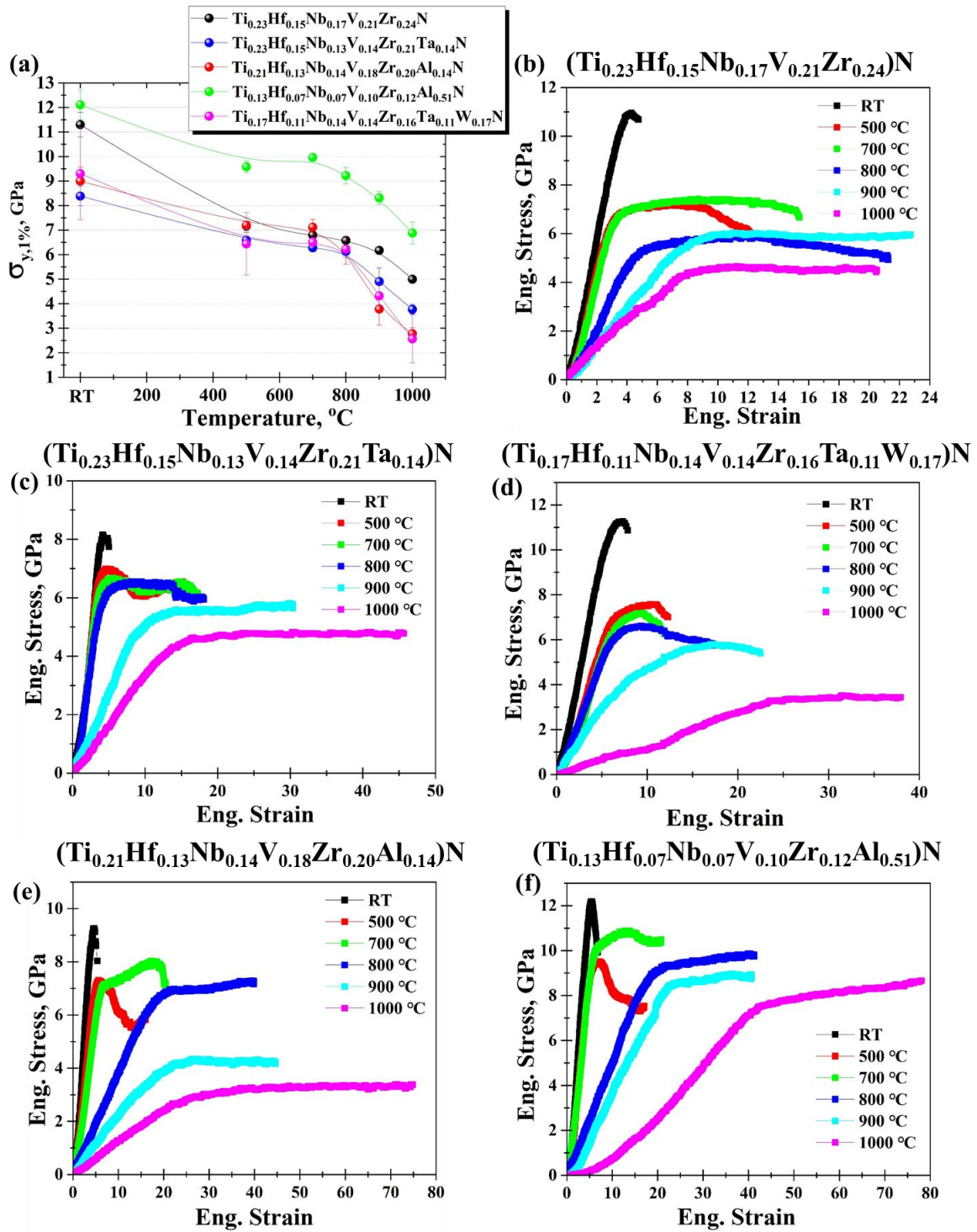


Fig. S10. The complete set of stress-strain curves for (a) $(\text{TiHfNbVZr})\text{N}$, (b) hexanary $(\text{TiHfNbVZrTa})\text{N}$, and (c) heptanary $(\text{TiHfNbVZrTaW})\text{N}$, (d) the hexanary Al-low and (e) Al-high $(\text{TiHfNbVZrAl})\text{N}$ systems compressed at RT, 500 °C, 700 °C, 800 °C, 900 °C, and 1000 °C. For a statistical accuracy at least 4-5 pillars are compressed for each film composition at each test temperature.

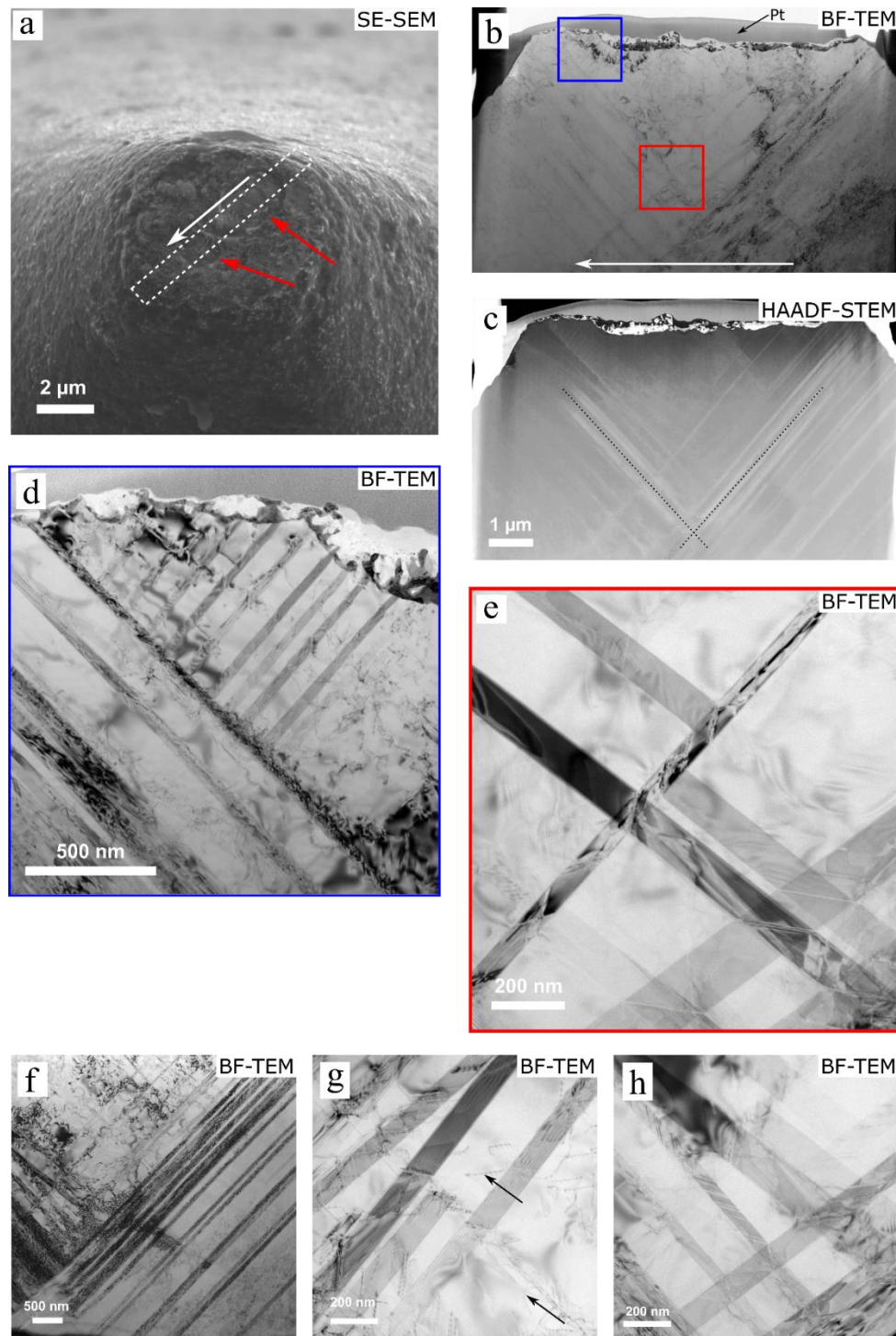


Fig. S11. (a) SEM image of the diamond punch after compression up to 1000 °C with pillar imprints arrowed in red and cross-section lift-out location indicated; (b, c) BF-TEM and STEM-HAADF overview images of the punch cross-section, oriented by the white arrows in (a, b), with major intersecting slip traces indicated (dotted black lines in (c)). BF-TEM images of the crystal deformation structures (d) in the region near the micropillar contact surface, indicated in (b), and (e - h) at the intersection of major stacking fault families, where the stacking fault density is high. Black arrows in (g) indicate ordinary dislocations.

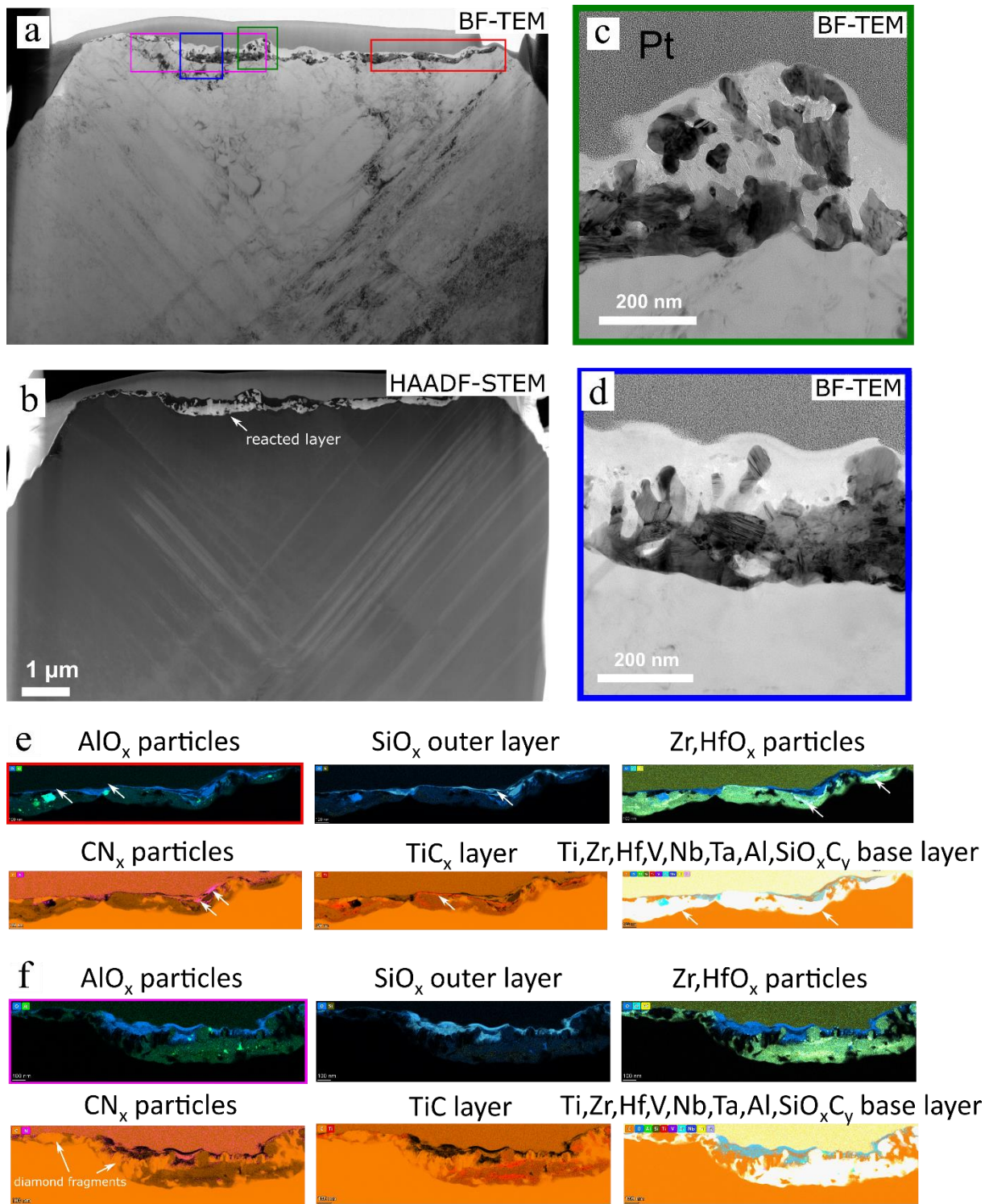


Fig. S12. (a, b) BF-TEM and STEM-HAADF overview images of the punch cross-section, (c, d) High magnification BF-TEM images of the reacted layer and (e, f) STEM-EDX analysis of the reaction products, indicated by white arrows in each case, observed in the cross-section of the diamond punch after compression up to 1000 °C, taken from the regions highlighted in (a).

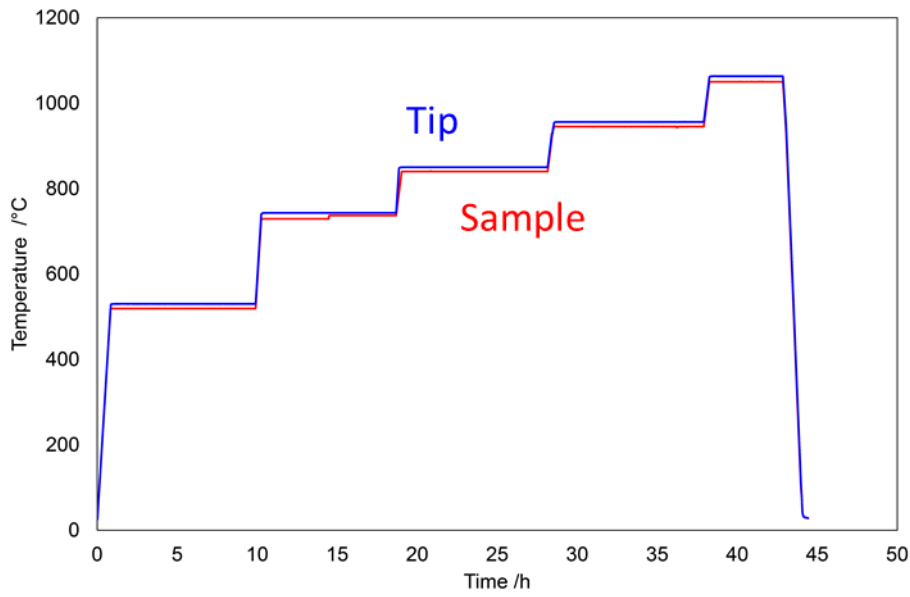


Fig. S13. Temperature profile of a representative high temperature microcompression experiment: measured temperatures of tip and sample side thermocouples.

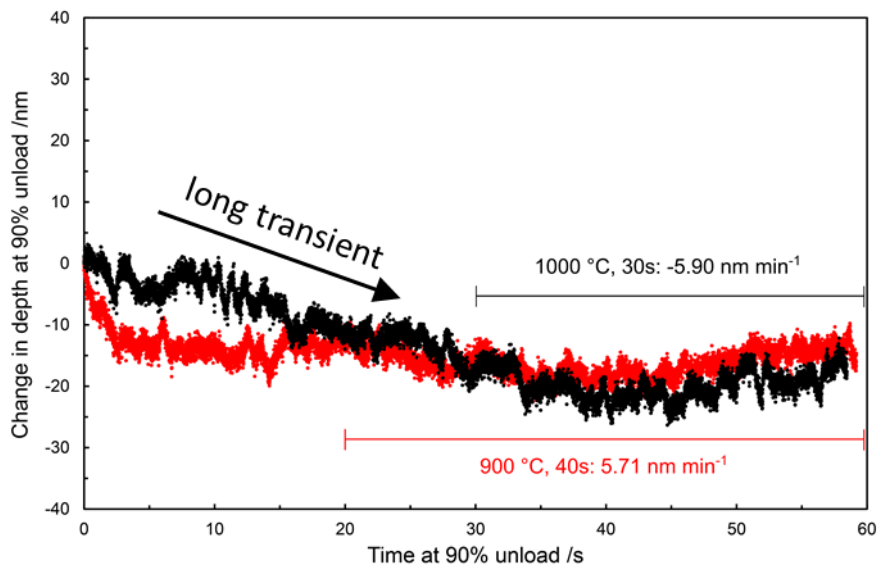


Fig. S14. Displacement drift curves at constant load (upon 90% unloading) for temperature matching at 900 and 1000 °C.

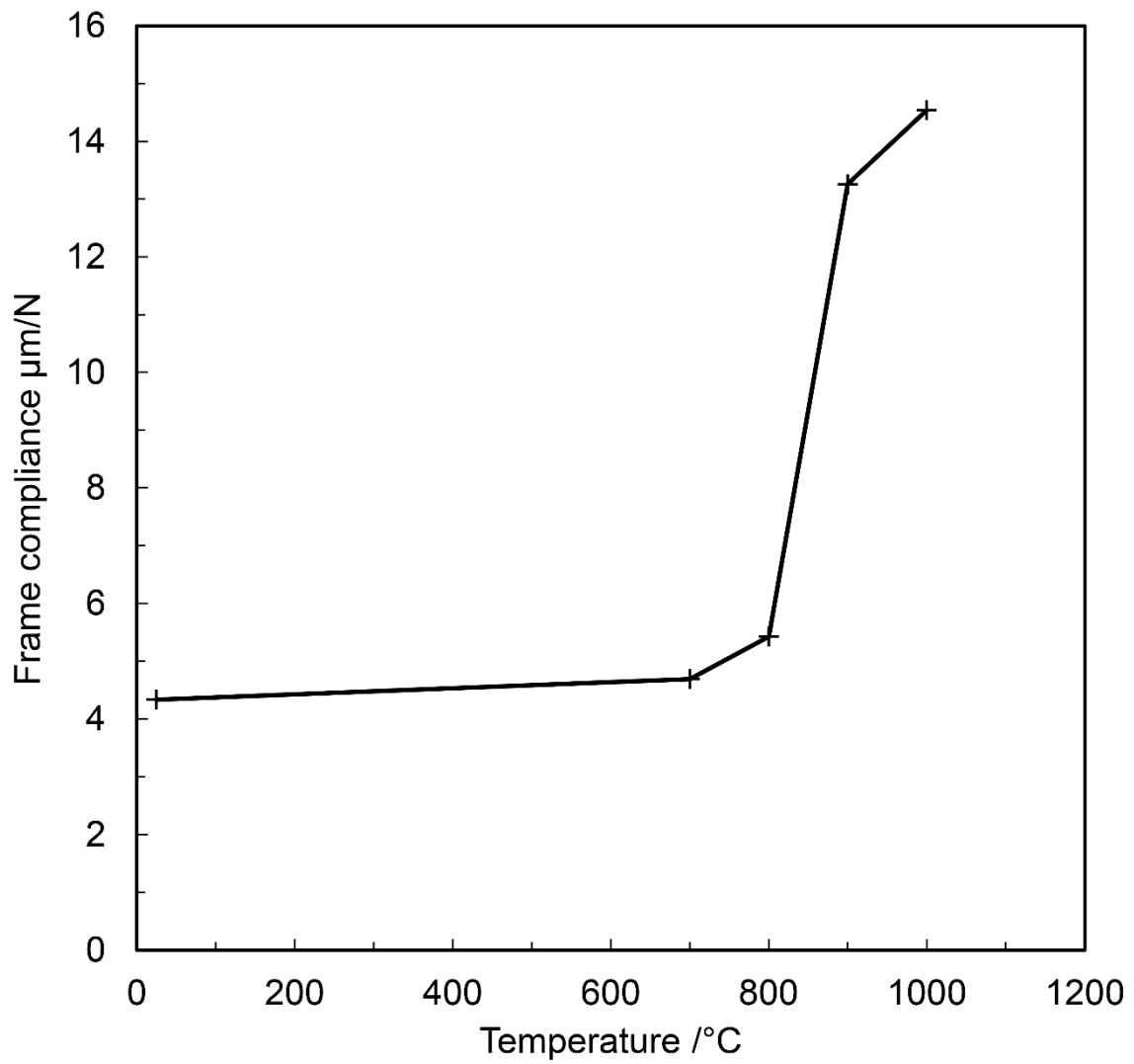


Fig. S15. Rig compliance of the high temperature nanoindentation setup against test temperature measured using a conductive diamond Berkovich on (0001) sapphire.

$(\text{Ti}_{0.17}\text{Hf}_{0.11}\text{Nb}_{0.14}\text{V}_{0.14}\text{Zr}_{0.16}\text{Ta}_{0.11}\text{W}_{0.17})\text{N}$
Pillar sample, near-surface area

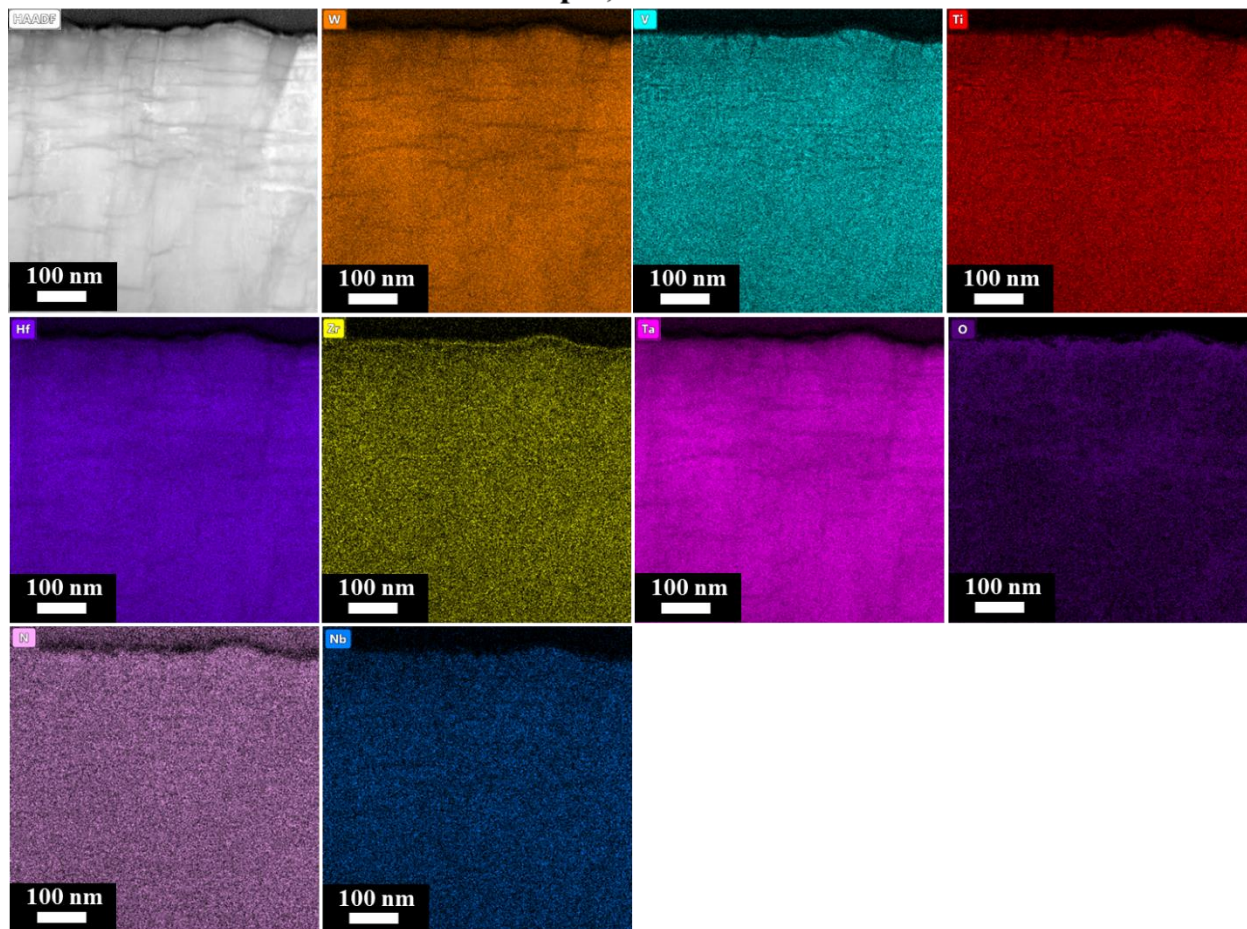


Fig. S16. Magnified STEM-EDX color-coded elemental maps acquired from the near surface area of the heptanary nitride film after micropillar compression tests at 1000 °C.

$(\text{Ti}_{0.17}\text{Hf}_{0.11}\text{Nb}_{0.14}\text{V}_{0.14}\text{Zr}_{0.16}\text{Ta}_{0.11}\text{W}_{0.17})\text{N}$
Pillar sample, middle-depth of the film

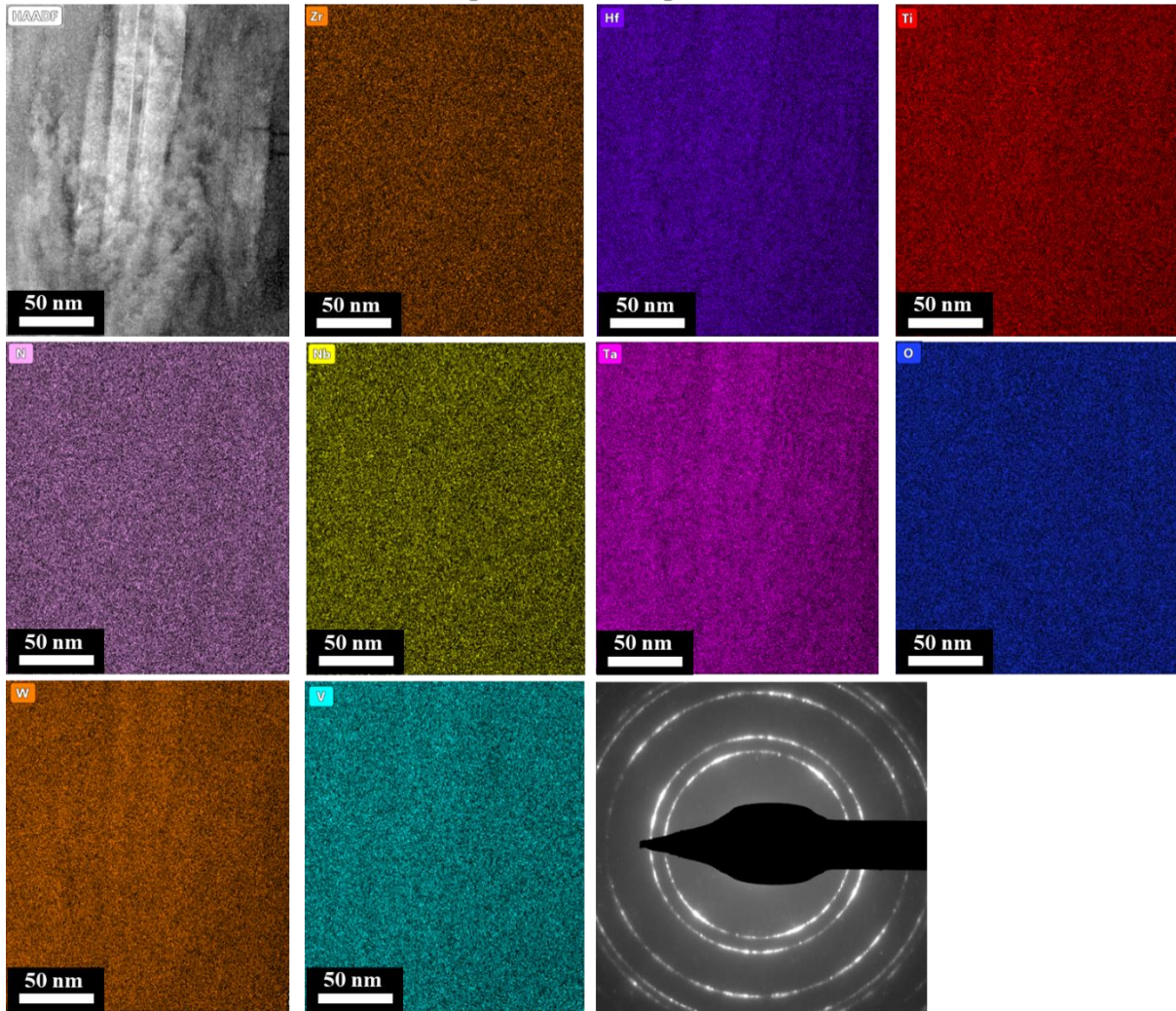


Fig. S17. Magnified STEM-EDX color-coded elemental maps acquired from the mid-depth of the heptanary nitride film after micropillar compression tests at 1000 °C and corresponding SAED.

$(\text{Ti}_{0.13}\text{Hf}_{0.07}\text{Nb}_{0.07}\text{V}_{0.10}\text{Zr}_{0.12}\text{Al}_{0.51})\text{N}$
1200 °C-compressed pillar

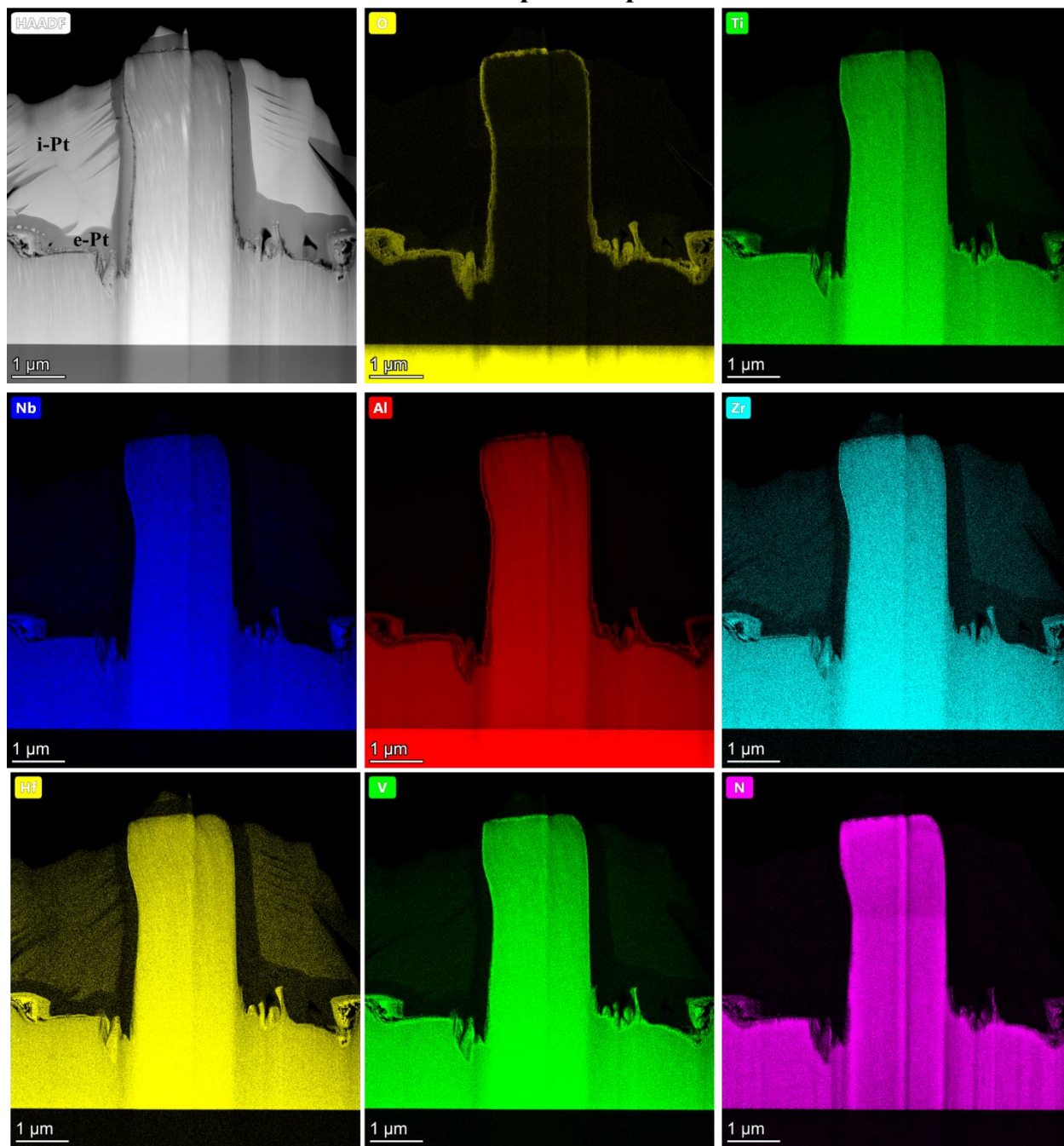


Fig. S18. STEM-EDX color-coded elemental maps acquired from the hexanary Al-high pillar after compression at 1000 °C.

$(\text{Ti}_{0.13}\text{Hf}_{0.07}\text{Nb}_{0.07}\text{V}_{0.10}\text{Zr}_{0.12}\text{Al}_{0.51})\text{N}$
1200 °C-compressed pillar

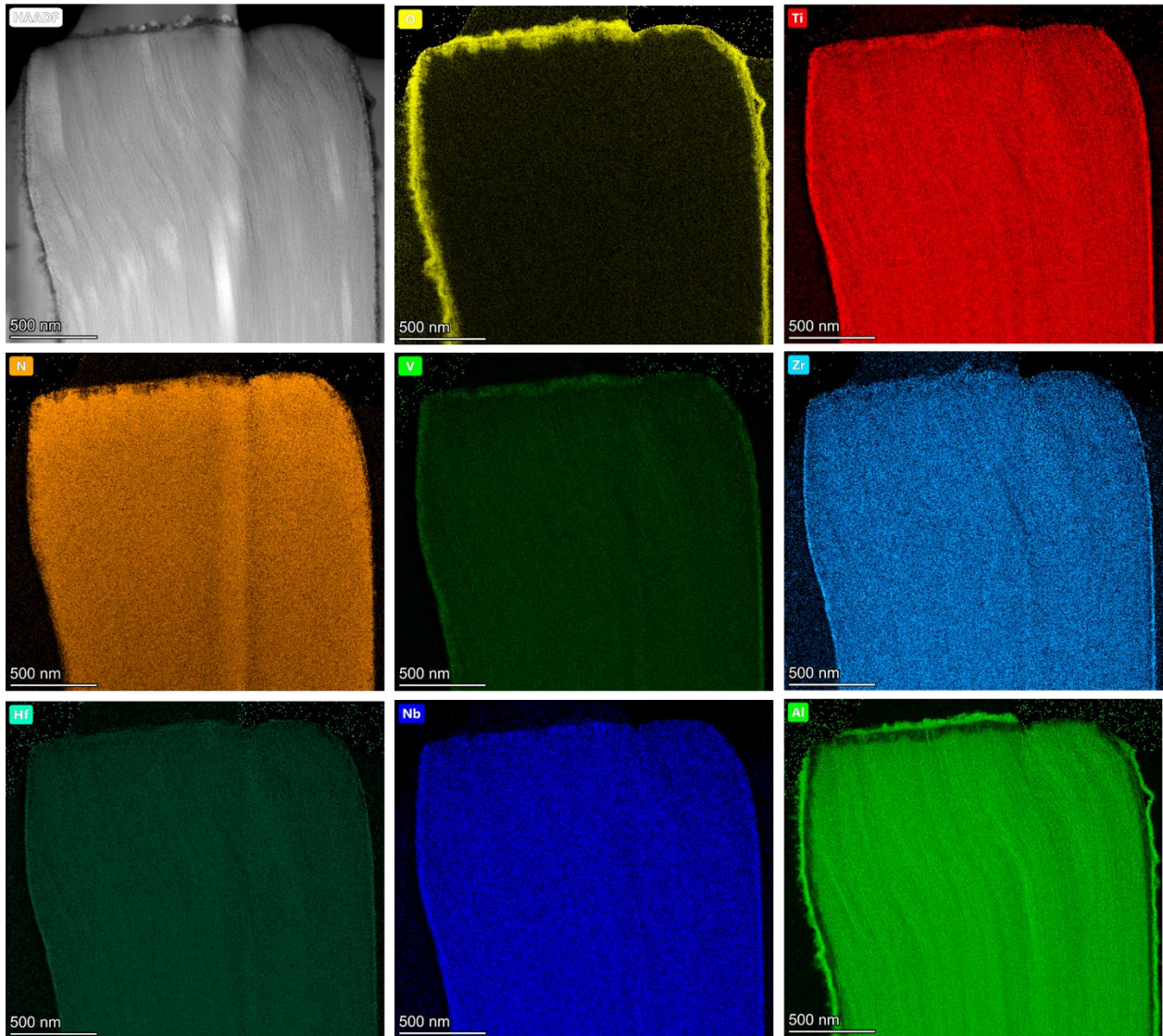


Fig. S19. STEM-EDX color-coded elemental maps acquired from the upper part of the hexanary Al-high pillar after compression at 1000 °C.

Additional References

1. Pshyk, A. V. *et al.* High-entropy transition metal nitride thin films alloyed with Al: Microstructure, phase composition and mechanical properties. *Mater. Des.* **219**, 110798 (2022).
2. Wheeler, J. M. & Michler, J. Elevated temperature, nano-mechanical testing in situ in the scanning electron microscope. *Rev. Sci. Instrum.* **84**, (2013).
3. Edwards, T. E. J. *et al.* Longitudinal twinning in a TiAl alloy at high temperature by in situ microcompression. *Acta Mater.* **148**, 202–215 (2018).
4. Oliver, W. C. C. & Pharr, G. M. M. Improved technique for determining hardness and elastic modulus using load and displacement sensing indentation experiments. *J. Mater. Res.* **7**, 1564–1580 (1992).
5. Schmid, F. & Harris, D. C. Effects of crystal orientation and temperature on the strength of sapphire. *J. Am. Ceram. Soc.* **81**, 885–893 (1998).
6. Wachtman, J. B. & Lam, D. G. Young's Modulus of Various Refractory Materials as a Function of Temperature. *J. Am. Ceram. Soc.* **42**, 254–260 (1959).
7. Zhang, H., Schuster, B. E., Wei, Q. & Ramesh, K. T. The design of accurate micro-compression experiments. *Scr. Mater.* **54**, 181–186 (2006).
8. Ong, S. P., Wang, L., Kang, B. & Ceder, G. Li - Fe - P - O₂ phase diagram from first principles calculations. *Chem. Mater.* **20**, 1798–1807 (2008).
9. Ong, S. P., Jain, A., Hautier, G., Kang, B. & Ceder, G. Thermal stabilities of delithiated olivine MPO₄ (M = Fe, Mn) cathodes investigated using first principles calculations. *Electrochem. commun.* **12**, 427–430 (2010).
10. Li, W., Liu, P. & Liaw, P. K. Microstructures and properties of high-entropy alloy films and coatings: A review. *Mater. Res. Lett.* **6**, 199–229 (2018).
11. Oses, C. High-entropy ceramics. *Nat. Rev. Mater.* **5**, 295–309 (2020).
12. Akrami, S., Edalati, P., Fuji, M. & Edalati, K. High-entropy ceramics : Review of principles , production and applications. *Mater. Sci. Eng. R* **146**, 100644 (2021).
13. Chang, H.-W. *et al.* Influence of substrate bias, deposition temperature and post-deposition annealing on the structure and properties of multi-principal-component (AlCrMoSiTi)N coatings. *Surf. Coatings Technol.* **202**, 3360–3366 (2008).
14. Huang, P. & Yeh, J. Inhibition of grain coarsening up to 1000 ° C in (AlCrNbSiTiV) N superhard coatings. *Scr. Mater.* **62**, 105–108 (2010).
15. Kretschmer, A. *et al.* Strain-stabilized Al-containing high-entropy sublattice nitrides. *Acta Mater.* **224**, 117483 (2022).
16. Yalamanchili, K. *et al.* Exploring the high entropy alloy concept in (AlTiVNbCr)N. *Thin Solid Films* **636**, 346–352 (2017).
17. Pickering, E. J. & Jones, N. G. High-entropy alloys: a critical assessment of their founding principles and future prospects. *Int. Mater. Rev.* **61**, 183–202 (2016).
18. Kirnbauer, A. *et al.* Mechanical properties and thermal stability of reactively sputtered

- multi- principal-metal Hf-Ta-Ti-V-Zr nitrides. *Surf. Coat. Technol.* **389**, 125674 (2020).
19. Feng, L., Chen, W. T., Fahrenholtz, W. G. & Hilmas, G. E. Strength of single-phase high-entropy carbide ceramics up to 2300°C. *J. Am. Ceram. Soc.* **104**, 419–427 (2021).
 20. Castle, E., Csanádi, T., Grasso, S., Dusza, J. & Reece, M. Processing and Properties of High- Entropy Ultra-High Temperature Carbides. *Sci. Rep.* **8**, 1–12 (2018).
 21. Sangiovanni, D. G., Mellor, W., Harrington, T., Kaufmann, K. & Vecchio, K. Enhancing plasticity in high-entropy refractory ceramics via tailoring valence electron concentration. *Mater. Des.* **209**, 109932 (2021).
 22. Demirskyi, D. *et al.* High-temperature flexural strength performance of ternary high-entropy carbide consolidated via spark plasma sintering of TaC, ZrC and NbC. *Scr. Mater.* **164**, 12–16 (2019).
 23. Han, X. *et al.* Improved creep resistance of high entropy transition metal carbides. *J. Eur. Ceram. Soc.* **40**, 2709–2715 (2020).
 24. Fahrenholtz, W. G. & Hilmas, G. E. Ultra-high temperature ceramics : Materials for extreme environments. *Scr. Mater.* **129**, 94–99 (2017).
 25. Mayrhofer, P. H., Kirnbauer, A., Ertelthaler, P. & Koller, C. M. High-entropy ceramic thin films; A case study on transition metal diborides. *Scr. Mater.* **149**, 93–97 (2018).
 26. Kirnbauer, A. *et al.* Thermal stability and mechanical properties of sputtered (Hf ,Ta ,V ,W ,Zr)-diborides. *Acta Mater.* **200**, 559–569 (2020).
 27. Kang, W., Merrill, M. & Wheeler, J. M. In situ thermomechanical testing methods for micro/nano-scale materials. *Nanoscale* **9**, 2666–2688 (2017).
 28. Wheeler, J. M. & Michler, J. Invited article: Indenter materials for high temperature nanoindentation. *Rev. Sci. Instrum.* **84**, 1–11 (2013).
 29. Yu, X. *et al.* Constitutive law and flow mechanism in diamond deformation. *Sci. Rep.* **2**, 1–7 (2012).